

1

<sup>2</sup>A SEARCH FOR LONG-LIVED, CHARGED, SUPERSYMMETRIC PARTICLES  
<sup>3</sup>USING IONIZATION WITH THE ATLAS DETECTOR

4

BRADLEY AXEN

5

September 2016 – Version 0.35

6



<sup>8</sup> Bradley Axen: *A Search for Long-Lived, Charged, Supersymmetric Particles using*  
<sup>9</sup> *Ionization with the ATLAS Detector*, Subtitle, © September 2016

10

Usually a quotation.

11

Dedicated to.



<sub>12</sub> ABSTRACT

---

<sub>13</sub> How to write a good abstract:

<sub>14</sub> <https://plg.uwaterloo.ca/~migod/research/beck00PSLA.html>

[ September 19, 2016 at 11:30 – Version 0.35 ]

<sub>15</sub> PUBLICATIONS

---

<sub>16</sub> Some ideas and figures have appeared previously in the following publications:

<sub>17</sub>

<sub>18</sub> Put your publications from the thesis here. The packages `multibib` or `bibtopic`  
<sub>19</sub> etc. can be used to handle multiple different bibliographies in your document.



---

<sup>21</sup> ACKNOWLEDGEMENTS

<sup>22</sup> Put your acknowledgements here.

<sup>23</sup>

<sup>24</sup> And potentially a second round.

<sup>25</sup>



26 CONTENTS

---

27	I	INTRODUCTION	1
28	1	INTRODUCTION	3
29	II	THEORETICAL CONTEXT	5
30	2	STANDARD MODEL	7
31	2.1	Particles . . . . .	7
32	2.2	Interactions . . . . .	8
33	2.3	Limitations . . . . .	8
34	3	SUPERSYMMETRY	9
35	3.1	Motivation . . . . .	9
36	3.2	Structure . . . . .	9
37	3.3	Phenomenology . . . . .	9
38	4	LONG-LIVED PARTICLES	11
39	4.1	Mechanisms . . . . .	11
40	4.1.1	Examples in Supersymmetry . . . . .	11
41	4.2	Phenomenology . . . . .	11
42	4.2.1	Disimilarities to Prompt Decays . . . . .	11
43	4.2.2	Characteristic Signatures . . . . .	11
44	III	EXPERIMENTAL STRUCTURE AND RECONSTRUCTION	13
45	5	THE LARGE HADRON COLLIDER	15
46	5.1	Injection Chain . . . . .	15
47	5.2	Design and Parameters . . . . .	15
48	5.3	Luminosity . . . . .	15
49	6	THE ATLAS DETECTOR	17
50	6.1	Coordinate System . . . . .	17
51	6.2	Magnetic Field . . . . .	17
52	6.3	Inner Detector . . . . .	17
53	6.3.1	Pixel Detector . . . . .	17
54	6.3.2	Semiconductor Tracker . . . . .	17
55	6.3.3	Transition Radiation Tracker . . . . .	17
56	6.4	Calorimetry . . . . .	17
57	6.4.1	Electromagnetic Calorimeters . . . . .	17
58	6.4.2	Hadronic Calorimeters . . . . .	17
59	6.4.3	Forward Calorimeters . . . . .	17
60	6.5	Muon Spectrometer . . . . .	17
61	6.6	Trigger . . . . .	17
62	6.6.1	Trigger Scheme . . . . .	17
63	6.6.2	Missing Transverse Energy Triggers . . . . .	17
64	7	EVENT RECONSTRUCTION	19
65	7.1	Tracks and Vertices . . . . .	19

66	7.1.1	Track Reconstruction . . . . .	19
67	7.1.2	Vertex Reconstruction . . . . .	19
68	7.2	Jets . . . . .	19
69	7.2.1	Topological Clustering . . . . .	19
70	7.2.2	Jet Energy Scale . . . . .	19
71	7.2.3	Jet Energy Scale Uncertainties . . . . .	19
72	7.2.4	Jet Energy Resolution . . . . .	19
73	7.3	Electrons . . . . .	19
74	7.3.1	Electron Identification . . . . .	19
75	7.4	Muons . . . . .	19
76	7.4.1	Muon Identification . . . . .	19
77	7.5	Missing Transverse Energy . . . . .	19
78	IV	CALORIMETER RESPONSE	21
79	8	RESPONSE MEASUREMENT WITH SINGLE HADRONS	23
80	8.1	Dataset and Simulation . . . . .	24
81	8.1.1	Data Samples . . . . .	24
82	8.1.2	Simulated Samples . . . . .	24
83	8.1.3	Event Selection . . . . .	24
84	8.2	Inclusive Hadron Response . . . . .	25
85	8.2.1	E/p Distribution . . . . .	25
86	8.2.2	Zero Fraction . . . . .	26
87	8.2.3	Neutral Background Subtraction . . . . .	27
88	8.2.4	Corrected Response . . . . .	29
89	8.2.5	Additional Studies . . . . .	31
90	8.3	Identified Particle Response . . . . .	34
91	8.3.1	Decay Reconstruction . . . . .	34
92	8.3.2	Identified Response . . . . .	35
93	8.3.3	Additional Species in Simulation . . . . .	37
94	8.4	Summary . . . . .	38
95	9	JET ENERGY RESPONSE AND UNCERTAINTY	41
96	9.1	Motivation . . . . .	41
97	9.2	Uncertainty Estimate . . . . .	41
98	9.3	Summary . . . . .	44
99	V	SEARCH FOR LONG-LIVED PARTICLES	47
100	10	LONG-LIVED PARTICLES IN ATLAS	49
101	10.1	Event Topology . . . . .	49
102	10.1.1	Detector Interactions . . . . .	50
103	10.1.2	Lifetime Dependence . . . . .	51
104	10.2	Simulation . . . . .	54
105	11	EVENT SELECTION	57
106	11.1	Trigger . . . . .	58
107	11.2	Kinematics and Isolation . . . . .	59
108	11.3	Particle Species Rejection . . . . .	63
109	11.4	Ionization . . . . .	65
110	11.4.1	Mass Estimation . . . . .	66

111	11.5 Efficiency . . . . .	67
112	12 BACKGROUND ESTIMATION	71
113	12.1 Background Sources . . . . .	71
114	12.2 Prediction Method . . . . .	72
115	12.3 Validation . . . . .	73
116	12.3.1 Closure in Simulation . . . . .	73
117	12.3.2 Validation Region in Data . . . . .	74
118	13 SYSTEMATIC UNCERTAINTIES AND RESULTS	77
119	13.1 Systematic Uncertainties . . . . .	77
120	13.2 Final Yields . . . . .	77
121	14 INTERPRETATION	79
122	14.1 Cross Sectional Limits . . . . .	79
123	14.2 Mass Limits . . . . .	79
124	14.3 Context for Long-Lived Searches . . . . .	79
125	<b>VI CONCLUSIONS</b>	81
126	15 SUMMARY AND OUTLOOK	83
127	15.1 Summary . . . . .	83
128	15.2 Outlook . . . . .	83
129	<b>VII APPENDIX</b>	85
130	A INELASTIC CROSS SECTION	87
131	B APPENDIX TEST	89
132	B.1 Appendix Section Test . . . . .	89
133	B.1.1 Appendix Subection Test . . . . .	89
134	B.2 A Table and Listing . . . . .	89
135	B.3 Some Formulas . . . . .	90
136	BIBLIOGRAPHY	93

137 LIST OF FIGURES

---

138	Figure 1	The particle content of the Standard Model (SM). . . . .	8
139	Figure 2	An illustration (a) of the $E/p$ variable used throughout this paper. The red energy deposits come from the charged particle targeted for measurement, while the blue energy deposits are from nearby neutral particles and must be subtracted. The same diagram (b) for the neutral-background selection, described in Section 8.2.3.	26
140			
141			
142			
143			
144			
145	Figure 3	The $E/p$ distribution and ratio of simulation to data for isolated tracks with (a) $ \eta  < 0.6$ and $1.2 < p/\text{GeV} < 1.8$ and (b) $ \eta  < 0.6$ and $2.2 < p/\text{GeV} < 2.8$ . . . . .	26
146			
147			
148	Figure 4	The fraction of tracks as a function (a, b) of momentum, (c, d) of interaction lengths with $E \leq 0$ for tracks with positive (on the left) and negative (on the right) charge. . . . .	28
149			
150			
151			
152	Figure 5	$\langle E/p \rangle_{\text{BG}}$ as a function of the track momentum for tracks with (a) $ \eta  < 0.6$ , (b) $0.6 <  \eta  < 1.1$ , and as a function of the track pseudorapidity for tracks with (c) $1.2 < p/\text{GeV} < 1.8$ , (d) $1.8 < p/\text{GeV} < 2.2$ . . . . .	29
153			
154			
155			
156	Figure 6	$\langle E/p \rangle_{\text{COR}}$ as a function of track momentum, for tracks with (a) $ \eta  < 0.6$ , (b) $0.6 <  \eta  < 1.1$ , (c) $1.8 <  \eta  < 1.9$ , and (d) $1.9 <  \eta  < 2.3$ . . . . .	30
157			
158			
159	Figure 7	$\langle E/p \rangle_{\text{COR}}$ calculated using LCW-calibrated topological clusters as a function of track momentum for tracks with (a) zero or more associated topological clusters or (b) one or more associated topological clusters. . . . .	31
160			
161			
162			
163	Figure 8	Comparison of the $\langle E/p \rangle_{\text{COR}}$ for tracks with (a) less than and (b) greater than 20 hits in the TRT. . . . .	32
164			
165	Figure 9	Comparison of the $\langle E/p \rangle_{\text{COR}}$ for (a) positive and (b) negative tracks as a function of track momentum for tracks with $ \eta  < 0.6$ . . . . .	32
166			
167			
168	Figure 10	Comparison of the $E/p$ distributions for (a) positive and (b) negative tracks with $0.8 < p/\text{GeV} < 1.2$ and $ \eta  < 0.6$ , in simulation with the FTFP_BERT and QGSP_BERT physics lists. . . . .	33
169			
170			
171			
172	Figure 11	Comparison of the response of the hadronic calorimeter as a function of track momentum (a) at the EM-scale and (b) after the LCW calibration. . . . .	33
173			
174			
175	Figure 12	Comparison of the response of the EM calorimeter as a function of track momentum (a) at the EM-scale and (b) with the LCW calibration. . . . .	34
176			
177			

178	Figure 13	The reconstructed mass peaks of (a) $K_S^0$ , (b) $\Lambda$ , and (c) $\bar{\Lambda}$ candidates. . . . .	35
179			
180	Figure 14	The $E/p$ distribution for isolated (a) $\pi^+$ , (b) $\pi^-$ , (c) proton, and (d) anti-proton tracks. . . . .	36
181			
182	Figure 15	The fraction of tracks with $E \leq 0$ for identified (a) $\pi^+$ and $\pi^-$ , and (b) proton and anti-proton tracks . . . . .	36
183			
184	Figure 16	The difference in $\langle E/p \rangle$ between (a) $\pi^+$ and $\pi^-$ (b) $p$ and $\pi^+$ , and (c) $\bar{p}$ and $\pi^-$ . . . . .	37
185			
186	Figure 17	$\langle E/p \rangle_{\text{COR}}$ as a function of track momentum for (a) $\pi^+$ tracks and (b) $\pi^-$ tracks. . . . .	38
187			
188	Figure 18	The ratio of the calorimeter response to single parti- cles of various species to the calorimeter response to $\pi^+$ with the physics list FTFP_BERT. . . . .	38
189			
190	Figure 19	The spectra of true particles inside anti- $k_t$ , $R = 0.4$ jets with (a) $90 < p_T/\text{GeV} < 100$ , (b) $400 < p_T/\text{GeV} <$ $500$ , and (c) $1800 < p_T/\text{GeV} < 2300$ . . . . .	42
191			
192	Figure 20	The jet energy scale ( <a>JES</a> ) uncertainty contributions, as well as the total <a>JES</a> uncertainty, as a function of jet $p_T$ for (a) $ \eta  < 0.6$ and (b) $0.6 <  \eta  < 1.1$ . . . . .	44
193			
194	Figure 21	The <a>JES</a> correlations as a function of jet $p_T$ and $ \eta $ for jets in the central region of the detector. . . . .	45
195			
196	Figure 22	A schematic diagram of an R-Hadron event with a life- time around 0.01 ns. The diagram includes one charged R-Hadron (solid blue), one neutral R-Hadron (dashed blue), Lightest Supersymmetric Particles ( <a>LSPs</a> ) (dashed green) and charged hadrons (solid orange). The pixel detector, calorimeters, and muon system are illustrated but not to scale. . . . .	51
197			
198	Figure 23	A schematic diagram of an R-Hadron event with a life- time around 4 ns. The diagram includes one charged R-Hadron (solid blue), one neutral R-Hadron (dashed blue), <a>LSPs</a> (dashed green) and a charged hadron (solid orange). The pixel detector, calorimeters, and muon system are illustrated but not to scale. . . . .	52
199			
200	Figure 24	A schematic diagram of an R-Hadron event with a life- time around 5 ns. The diagram includes one charged R-Hadron (solid blue), one neutral R-Hadron (dashed blue), <a>LSPs</a> (dashed green) and charged hadrons (solid orange). The pixel detector, calorimeters, and muon system are illustrated but not to scale. . . . .	53
201			
202	Figure 25	A schematic diagram of an R-Hadron event with a life- time around 20 ns. The diagram includes one charged R-Hadron (solid blue), one neutral R-Hadron (dashed blue), <a>LSPs</a> (dashed green) and charged hadrons (solid orange). The pixel detector, calorimeters, and muon system are illustrated but not to scale. . . . .	53
203			
204			
205			
206			
207			
208			
209			
210			
211			
212			
213			
214			
215			
216			
217			
218			
219			
220			
221			
222			
223			

224	Figure 26	A schematic diagram of an R-Hadron event with a life-time around 20 ns. The diagram includes one charged R-Hadron (solid blue) and one neutral R-Hadron (dashed blue). The pixel detector, calorimeters, and muon system are illustrated but not to scale. . . . .	54
225			
226			
227			
228			
229	Figure 27	The distribution of $E_T^{\text{miss}}$ for data and simulated signal events, after the trigger requirement. . . . .	59
230			
231	Figure 28	The trigger efficiency for the HLT_xe70 trigger requirement as a function of (a) $E_T^{\text{miss}}$ and (b) Calorimeter $E_T^{\text{miss}}$ for simulated signal events. Data events with a W boson selection and simulated W boson events are also included. . . . .	60
232			
233			
234			
235			
236	Figure 29	The dependence of $dE/dx$ on $N_{\text{split}}$ in data after basic track hit requirements have been applied. . . . .	61
237			
238	Figure 30	The distribution of $dE/dx$ with various selections applied in data and simulated signal events. . . . .	62
239			
240	Figure 31	The distribution of track momentum for data and simulated signal events, after previous selection requirements have been applied. . . . .	63
241			
242			
243	Figure 32	The distribution of $M_T$ for data and simulated signal events, after previous selection requirements have been applied. . . . .	64
244			
245			
246	Figure 33	The distribution of summed tracked momentum within a cone of $\Delta R < 0.25$ around the candidate track for data and simulated signal events, after previous selection requirements have been applied. . . . .	64
247			
248			
249			
250	Figure 34	The normalized, two-dimensional distribution of $E/p$ and $f_{\text{EM}}$ for simulated (a) $Z \rightarrow ee$ , (b) $Z \rightarrow \tau\tau$ , (c) 1200 GeV Stable R-Hadron events, and (d) 1200 GeV, 10 ns R-Hadron events. . . . .	66
251			
252			
253			
254	Figure 35	Two-dimensional distribution of $dE/dx$ versus charge signed momentum ( $qp$ ) for minimum-bias tracks. The fitted distributions of the most probable values for pions, kaons and protons are superimposed. . . . .	67
255			
256			
257			
258	Figure 36	The distribution of mass estimated using $dE/dx$ for simulated stable R-Hadrons with masses between 1000 and 1600 GeV. . . . .	68
259			
260			
261	Figure 37	The acceptance $\times$ efficiency as a function of R-Hadron (a) mass and (b) lifetime. (a) shows all of the combinations of mass and lifetime considered in this search, and (b) highlights the lifetime dependence for 1000 GeV and 1600 GeV R-Hadrons. . . . .	68
262			
263			
264			
265			

266	<b>Figure 38</b>	The distribution of (a) $dE/dx$ and (b) momentum for tracks in data and simulated signal after requiring the event level selection and the track selection on $p_T$ , hits, and $N_{\text{split}}$ . Each sub-figure shows the normalized distributions for tracks classified as hadrons, electrons, and muons in data and R-Hadrons in the simulated signal. . . . .	72
267			
268			
269			
270			
271			
272			
273	<b>Figure 39</b>	The distribution of $M_{dE/dx}$ (a) before and (b) after the ionization requirement for tracks in simulated W boson decays and for the randomly generated background estimate. . . . .	74
274			
275			
276			
277	<b>Figure 40</b>	The distribution of $M_{dE/dx}$ (a) before and (b) after the ionization requirement for tracks in the validation region and for the randomly generated background estimate. . . . .	75
278			
279			
280			

281 LIST OF TABLES

---

<small>282</small>	Table 1	The dominant sources of corrections and systematic uncertainties in the JES estimation technique, including typical values for the correcting shift ( $\Delta$ ) and the associated uncertainty ( $\sigma$ ). . . . .	<small>43</small>
<small>283</small>			
<small>284</small>			
<small>285</small>			
<small>286</small>	Table 2	The expected number of events at each level of the selection for metastable 1600 GeV, 10 ns R-Hadrons, along with the number of events observed in data, for $3.2 \text{ fb}^{-1}$ . The simulated yields are shown with statistical uncertainties only. The total efficiency $\times$ acceptance is also shown for the signal. . . . .	<small>69</small>
<small>287</small>			
<small>288</small>			
<small>289</small>			
<small>290</small>			
<small>291</small>			
<small>292</small>	Table 3	Autem usu id . . . . .	<small>89</small>

<sub>293</sub> LISTINGS

---

<sub>294</sub> Listing 1	A floating example ( <code>listings</code> manual)	90
--------------------------	--	----

295 ACRONYMS

---

- 296 SM Standard Model  
297 SUSY Supersymmetry  
298 LSP Lightest Supersymmetric Particle  
299 LHC Large Hadron Collider  
300 ATLAS A Toroidal LHC ApparatuS  
301 ToT time over threshold  
302 LCW local cluster weighted  
303 MIP minimally ionizing particle  
304 EPJC European Physical Journal C  
305 JES jet energy scale  
306 LLP Long-Lived Particle  
307 CR Control Region  
308 NLO next-to-leading order  
309 NLL next-to-leading logarithmic  
310 PDF parton distribution function  
311 ISR initial state radiation

312

## PART I

313

### INTRODUCTION

314

You can put some informational part preamble text here.



# 1

315

## 316 INTRODUCTION

---



317

## PART II

318

### THEORETICAL CONTEXT

319

You can put some informational part preamble text here.



# 2

320

## 321 STANDARD MODEL

---

322 The SM of particle physics seeks to explain the symmetries and interactions of  
323 all currently discovered fundamental particles. It has been tested by several genera-  
324 tions of experiments and has been remarkably successful, no significant de-  
325 viations have been found. The SM provides predictions in particle physics for  
326 interactions up to the Planck scale ( $10^{15}$ - $10^{19}$  GeV).

327 The theory itself is a quantum field theory grown from an underlying  $SU(3) \times$   
328  $SU(2) \times U(1)$  that requires the particle content and quantum numbers consist-  
329 ent with experimental observations (see Section 2.1). Each postulated symme-  
330 try is accompanied by an interaction between particles through gauge invari-  
331 ance. These interactions are referred to as the Strong, Weak, and Electromag-  
332 netic forces, which are discussed in Section 2.2.

333 Although this model has been very predictive, the theory is incomplete; for  
334 example, it is not able to describe gravity or astronomically observed dark matter.  
335 These limitations are discussed in more detail in Section 2.3.

## 336 21 PARTICLES

337 The most familiar matter in the universe is made up of protons, neutrons, and  
338 electrons. Protons and neutrons are composite particles, however, and are made  
339 up in turn by particles called quarks. Quarks carry both electric charge and color  
340 charge, and are bound in color-neutral combinations called baryons. The elec-  
341 tron is an example of a lepton, and carries only electric charge. Another type  
342 of particle, the neutrino, does not form atomic structures in the same way that  
343 quarks and leptons do because it carries no color or electric charge. Collectively,  
344 these types of particles are known as fermions, the group of particles with half-  
345 integer spin.

346 There are three generations of fermions, although familiar matter is formed  
347 predominantly by the first generation. The generations are identical except for  
348 their masses, which increase in each generation by convention. In addition, each  
349 of these particles is accompanied by an antiparticle, with opposite-sign quantum  
350 numbers but the same mass.

351 The fermions comprise what is typically considered matter, but there are  
352 additional particles that are mediators of interactions between those fermions.  
353 These mediators are known as the gauge bosons, gauge in that their existence  
354 is required by gauge invariance (discussed further in Section 2.2) and bosons in  
355 that they have integer spin. The boson which mediates the electromagnetic force  
356 is the photon, the first boson to be discovered; it has no electric charge, no mass,  
357 and a spin of 1. There are three spin-1 mediators of the weak force, the two  
358 W bosons and the Z boson. The W bosons have electric charge of  $\pm 1$  and a  
359 mass of  $80.385 \pm 0.015$  GeV, while the Z boson is neutral and has a mass of

360 91.1876  $\pm$  0.0021 GeV. The strong force is mediated by eight particles called  
 361 gluons, which are massless and electrically neutral but do carry color charge.

362 The final particle present in the SM is the Higgs boson, which was recently  
 363 observed for the first time by experiments at CERN in 2012. It is electrically  
 364 neutral, has a mass of 125.7  $\pm$  0.4 GeV, and is the only spin-0 particle yet to be  
 365 observed. The Higgs boson is the gauge boson associated with the mechanism  
 366 that gives a mass to the W and Z bosons.

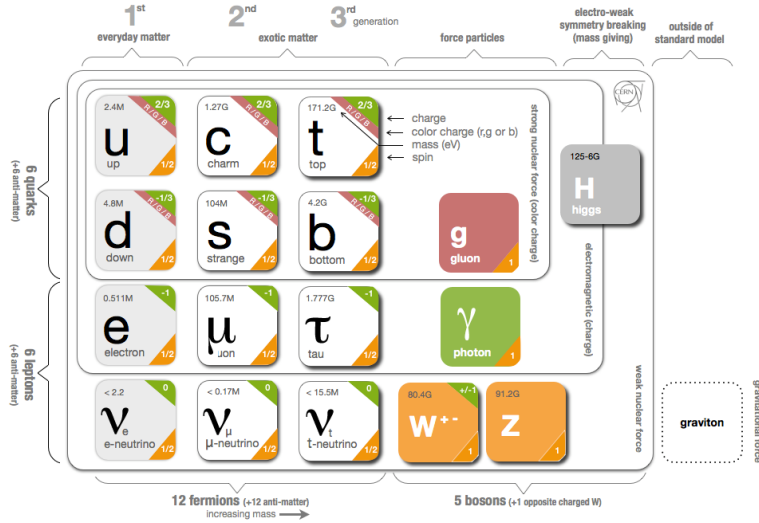


Figure 1: The particle content of the SM.

367 Together these particles form the entire content of the SM, and are summa-  
 368 rized in Figure 1. These are the particles that constitute the observable universe  
 369 and all the so-far-observed interactions within it.

## 370 2.2 INTERACTIONS

371 The interactions predicted and described by the SM are fundamentally tied to the  
 372 particles within it, both in that they describe the way those particles can influence  
 373 each other and also in that the existence of the interactions requires the existence  
 374 of some particles (the gauge bosons).

## 375 2.3 LIMITATIONS

# 3

376

377 SUPERSYMMETRY

---

378 3.1 MOTIVATION

379 3.2 STRUCTURE

380 3.3 PHENOMENOLOGY



# 4

381

382 LONG-LIVED PARTICLES

---

383 4.1 MECHANISMS

384 4.1.1 EXAMPLES IN SUPERSYMMETRY

385 4.2 PHENOMENOLOGY

386 4.2.1 DISIMILARITIES TO PROMPT DECAYS

387 4.2.2 CHARACTERISTIC SIGNATURES



388

### PART III

389

## EXPERIMENTAL STRUCTURE AND RECONSTRUCTION

390

You can put some informational part preamble text here.



# 5

391

392 THE LARGE HADRON COLLIDER

---

393 5.1 INJECTION CHAIN

394 5.2 DESIGN AND PARAMETERS

395 5.3 LUMINOSITY



# 6

396

## 397 THE ATLAS DETECTOR

---

398 6.1 COORDINATE SYSTEM

399 6.2 MAGNETIC FIELD

400 6.3 INNER DETECTOR

401 6.3.1 PIXEL DETECTOR

402 6.3.2 SEMICONDUCTOR TRACKER

403 6.3.3 TRANSITION RADIATION TRACKER

404 6.4 CALORIMETRY

405 6.4.1 ELECTROMAGNETIC CALORIMETERS

406 6.4.2 HADRONIC CALORIMETERS

407 6.4.3 FORWARD CALORIMETERS

408 6.5 MUON SPECTROMETER

409 6.6 TRIGGER

410 6.6.1 TRIGGER SCHEME

411 6.6.2 MISSING TRANSVERSE ENERGY TRIGGERS



# 7

412

## 413 EVENT RECONSTRUCTION

---

414 The ATLAS experiment combines measurements in the subdetectors to form a  
415 cohesive picture of each physics event.

### 416 7.1 TRACKS AND VERTICES

#### 417 7.1.1 TRACK RECONSTRUCTION

##### 418 7.1.1.1 NEURAL NETWORK

##### 419 7.1.1.2 PIXEL DE/DX

#### 420 7.1.2 VERTEX RECONSTRUCTION

### 421 7.2 JETS

#### 422 7.2.1 TOPOLOGICAL CLUSTERING

#### 423 7.2.2 JET ENERGY SCALE

#### 424 7.2.3 JET ENERGY SCALE UNCERTAINTIES

#### 425 7.2.4 JET ENERGY RESOLUTION

### 426 7.3 ELECTRONS

#### 427 7.3.1 ELECTRON IDENTIFICATION

### 428 7.4 MUONS

#### 429 7.4.1 MUON IDENTIFICATION

### 430 7.5 MISSING TRANSVERSE ENERGY



431

## PART IV

432

### CALORIMETER RESPONSE

433

You can put some informational part preamble text here.



# 8

434

## 435 RESPONSE MEASUREMENT WITH SINGLE HADRONS

---

436 As discussed in Section 7.2, colored particles produced in collisions hadronize  
437 into jets of multiple hadrons. One approach to understanding jet energy mea-  
438 surements in the ATLAS calorimeters is to evaluate the calorimeter response to  
439 those individual hadrons; measurements of individual hadrons can be used to  
440 build up an understanding of the jets that they form. The redundancy of the  
441 momentum provided by the tracking system and the energy provided by the  
442 calorimeter provides an opportunity to study calorimeter response using real  
443 collisions, as described further in Section 8.2.

444 Calorimeter response includes a number of physical effects that can be ex-  
445 tracted to provide insight into many aspects of jet modeling. First, many charged  
446 hadrons interact with the material of the detector prior to reaching the calorime-  
447 ters and thus do not deposit any energy. Comparing this effect in data and simu-  
448 lation is a powerful tool in validating the interactions of particles with the mate-  
449 rial of the detector and the model of the detector geometry in simulation, see Sec-  
450 tion 8.2.2. The particles which do reach the calorimeter deposit their energy into  
451 several adjacent cells, which are then clustered together. The energy of the clus-  
452 ter is then the total energy deposited by that particle. Comparing the response of  
453 hadrons in data to that of simulated hadrons provides a direct evaluation of the  
454 showering of hadronic particles and the energy deposited by particles in matter  
(Section 8.2.4).

455 The above studies all use an inclusive selection of charged particles, which are  
456 comprised predominantly of pions, kaons, and (anti)protons. It is also possible to  
457 measure the response to various identified particle types separately to evaluate  
458 the simulated interactions of each particle, particularly at low energies where  
459 differences between species are very relevant. Pions and (anti)protons can be  
460 identified through decays of long-lived particles, in particular  $\Lambda$ ,  $\bar{\Lambda}$ , and  $K_S^0$ , and  
461 then used to measure response as described above. This is discussed in detail in  
462 Section 8.3.

463 The results in this chapter use data collected at 7 and 8 TeV collected in 2010  
464 and 2012, respectively. Both are included as the calorimeter was repaired and  
465 recalibrated between those two data-taking periods. Both sets of data are com-  
466 pared to an updated simulation that includes new physics models provided by  
467 Geant4 [1] and improvements in the detector description [2, 3]. The present  
468 results are published in European Physical Journal C (EPJC) [4] and can be com-  
469 pared to a similar measurement performed in 2009 and 2010 [5], which used the  
470 previous version of the simulation framework [6].

472 8.1 DATASET AND SIMULATION

473 8.1.1 DATA SAMPLES

474 The two datasets used in this chapter are taken from dedicated low-pileup runs  
 475 where the fraction of events with multiple interactions was negligible. These  
 476 datasets are used rather than those containing full-pileup events to facilitate mea-  
 477 surement of isolated hadrons. The 2012 dataset at  $\sqrt{s} = 8$  TeV contains 8 mil-  
 478 lion events and corresponds to an integrated luminosity of  $0.1 \text{ nb}^{-1}$ . The 2010  
 479 dataset at  $\sqrt{s} = 7$  TeV contains 3 million events and corresponds to an inte-  
 480 grated luminosity of  $3.2 \text{ nb}^{-1}$ . The latter dataset was also used for the 2010 re-  
 481 sults [5], but it has since been reanalyzed with an updated reconstruction includ-  
 482 ing the final, best understanding of the detector description for the material and  
 483 alignment from Run 1.

484 8.1.2 SIMULATED SAMPLES

485 The two datasets above are compared to simulated single-, double-, and non-  
 486 diffractive events generated with Pythia8 [7] using the A2 configuration of  
 487 hadronization [8] and the MSTW 2008 parton-distribution function set [9, 10].  
 488 The admixture of the single-, double-, and non-diffractive events uses the default  
 489 relative contributions from Pythia8. The conditions and energies for the two  
 490 simulations are chosen so that they match those of the corresponding dataset.

491 To evaluate the interaction of hadrons with detector material, the simulation  
 492 uses two different collections of hadronic physics models, called physics lists, in  
 493 Geant4 9.4 [11]. The first, QGSP\_BERT, combines the Bertini intra-nuclear  
 494 cascade [12–14] below 9.9 GeV, a parametrized proton inelastic model from 9.5  
 495 to 25 GeV [15], and a quark-gluon string model above 12 GeV [16–20]. The  
 496 second, FTFP\_BERT, combines the Bertini intra-nuclear cascade [12–14] below  
 497 5 GeV and the Fritiof model [21–24] above 4 GeV. In either list, Geant4 en-  
 498 forces a smooth transition between models where multiple models overlap.

499 8.1.3 EVENT SELECTION

500 The event selection for this study is minimal, as the only requirement is selecting  
 501 good-quality events with an isolated track. Such events are triggered by requir-  
 502 ing at least two hits in the minimum-bias trigger scintillators. After trigger, each  
 503 event is required to have exactly one reconstructed vertex, and that vertex is re-  
 504 quired to have four or more associated tracks.

505 The particles which are selected for the response measurements are first iden-  
 506 tified as tracks in the inner detector. The tracks are required to have at least 500  
 507 MeV of transverse momentum. To ensure a reliable momentum measurement,  
 508 these tracks are required to have at least one hit in the pixel detector, six hits in  
 509 the SCT, and small longitudinal and transverse impact parameters with respect  
 510 to the primary vertex [5]. For the majority of the measurements in this chapter,  
 511 the track is additionally required to have 20 hits in the TRT, which significantly

512 reduces the contribution from tracks which undergo nuclear interactions. This  
 513 requirement and its effect is discussed in more detail in Section 8.2.5. In addition,  
 514 tracks are rejected if there is any other reconstructed track which extrapolates  
 515 to the calorimeter within a cone of  $\Delta R = \sqrt{(\Delta\phi)^2 + (\Delta\eta)^2} < 0.4$ . This require-  
 516 ment guarantees that the contamination of energy from nearby charged particles  
 517 is negligible [5].

## 518 8.2 INCLUSIVE HADRON RESPONSE

519 The calorimeter response is more precisely defined as the ratio of the measured  
 520 calorimeter energy to the true energy carried by the particle, although this true  
 521 energy is unknown. For charged particles, however, the inner detector provides  
 522 a very precise measurement of momentum (with uncertainty less than 1%) that  
 523 can be used as a proxy for true energy. The ratio of the energy deposited by  
 524 the charged particle in the calorimeter,  $E$ , to its momentum measured in the  
 525 inner detector  $p$ , forms the calorimeter response measure called  $E/p$ . Though  
 526 the distribution of  $E/p$  contains a number of physical features, this study focuses  
 527 on the trends in two aggregated quantities:  $\langle E/p \rangle$ , the average of  $E/p$  for the  
 528 selected tracks, and the zero fraction, the fraction of tracks with no associated  
 529 energy in the calorimeter for those tracks.

530 The calorimeter energy assigned to a track is defined using clusters. The clus-  
 531 ters are formed using a 4–2–0 algorithm [25] that begins with seeds requiring  
 532 at least 4 times the average calorimeter cell noise. The neighboring cells with  
 533 at least twice that noise threshold are then added to the cluster, and all bound-  
 534 ing cells are then added with no requirement. This algorithm minimizes noise  
 535 contributions through its seeding process, and including the bounding cells im-  
 536 proves the energy resolution [26]. The clusters are associated to a given track  
 537 if they fall within a cone of  $\Delta R = 0.2$  of the extrapolated position of the track,  
 538 which includes about 90% of the energy on average [5]. This construction is il-  
 539 lustrated in Figure 2.

### 540 8.2.1 E/P DISTRIBUTION

541 The  $E/p$  distributions measured in both data and simulation are shown in Fig-  
 542 ure 3 for two example bins of track momentum and for tracks in the central  
 543 region of the detector. These distributions show several important features of  
 544 the  $E/p$  observable. The large content in the bin at  $E = 0$  comes from tracks that  
 545 have no associated cluster, which occurs due to interactions with detector mate-  
 546 rial prior to reaching the calorimeter or the energy deposit being insufficiently  
 547 large to generate a seed, and are discussed in Section 8.2.2. The small negative  
 548 tail also comes from tracks that do not deposit any energy in the calorimeter but  
 549 are randomly associated to a cluster with an energy below the noise threshold.  
 550 The long positive tail above 1.0 comes from the contribution of neutral parti-  
 551 cles. Nearby neutral particles deposit (sometimes large) additional energy in the  
 552 calorimeter but do not produce tracks in the inner detector, so they cannot be  
 553 rejected by the track isolation requirement. Additionally the peak and mean of

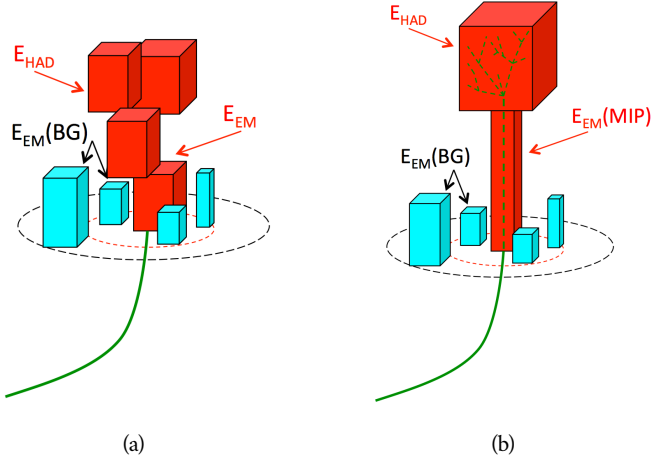


Figure 2: An illustration (a) of the  $E/p$  variable used throughout this paper. The red energy deposits come from the charged particle targeted for measurement, while the blue energy deposits are from nearby neutral particles and must be subtracted. The same diagram (b) for the neutral-background selection, described in Section 8.2.3.

the distribution falls below 1.0 because of the loss of energy not found within the cone as well as the non-compensation of the calorimeter.

The data and simulation share the same features, but the high and low tails are significantly different. The simulated events tend to overestimate the contribution of neutral particles to the long tail, an effect which can be isolated and removed as discussed in Section 8.2.3. Additionally, the simulated clusters have less noise on average, although this is a small effect on the overall response.

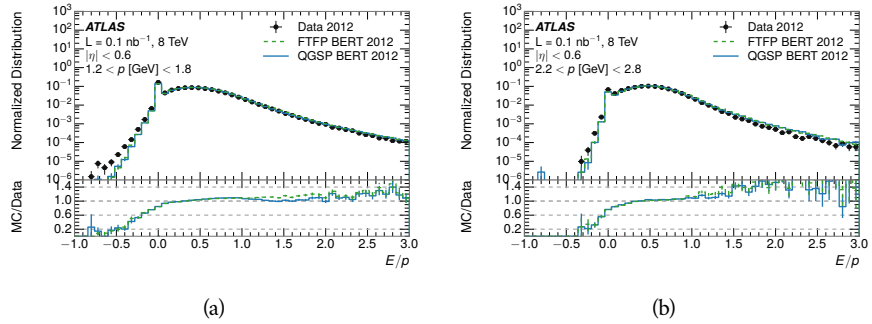


Figure 3: The  $E/p$  distribution and ratio of simulation to data for isolated tracks with (a)  $|\eta| < 0.6$  and  $1.2 < p/\text{GeV} < 1.8$  and (b)  $|\eta| < 0.6$  and  $2.2 < p/\text{GeV} < 2.8$ .

### 8.2.2 ZERO FRACTION

The fraction of particles with no associated clusters, or similarly those with  $E \leq 0$ , reflects the modeling of both the detector geometry and hadronic interactions. The zero fraction is expected to rise as the amount of material a particle traverses

increases, while it is expected to decrease as the particle energy increases. This dependence can be seen in Figure 4, where the zero fraction in data and simulation is shown as a function of momentum and the amount of material measured in interaction lengths. The trends are similar between 2010 and 2012 and for positively and negatively charged particles. The zero fraction decreases with energy as expected. The absolute discrepancy in zero fraction decreases with momentum from 5% to less than 1%, but this becomes more pronounced in the ratio as the zero fraction shrinks quickly with increasing momentum. There is a small constant difference between the data and simulation in both interaction models that becomes more pronounced. The amount of material in the detector increases with  $\eta$ , which is used to obtain results for interaction lengths ranging between 0.1 and 0.65  $\lambda$ . As the data and simulation have significant disagreement in the zero fraction over a number of interaction lengths, the difference must be primarily from the modeling of hadronic interactions with detector material and not just the detector geometry. Although two different hadronic interaction models are shown in the figure, they have very similar discrepancies to data because both use the same description (the BERT model) at low momentum.

### 8.2.3 NEUTRAL BACKGROUND SUBTRACTION

The isolation requirement on hadrons is only effective in removing an energy contribution from nearby charged particles. Nearby neutral particles, predominantly photons from  $\pi^0$  decays, also add their energy to the calorimeter clusters, but mostly in the electromagnetic calorimeter. It is possible to measure this contribution, on average, using late-showering hadrons that minimally ionize in the electromagnetic calorimeter. Such particles are selected by requiring that they deposit less than 1.1 GeV in the EM calorimeter within a cone of  $\Delta R < 0.1$  around the track. To ensure that these particles are well measured, they are additionally required to deposit between 40% and 90% of their energy in the hadronic calorimeter within the same cone.

These particles provide a clean sample to measure the nearby neutral background because they do not deposit energy in the area immediately surrounding them in the EM calorimeter, as shown in Figure 2. So, the energy deposits in the region  $0.1 < \Delta R < 0.2$  can be attributed to neutral particles alone. To estimate the contribution to the whole cone considered for the response measurement, that energy is scaled by a geometric factor of 4/3. This quantity,  $\langle E/p \rangle_{BG}$ , measured in aggregate over a number of particles, gives the contribution to  $\langle E/p \rangle$  from neutral particles in the EM calorimeter. Similar techniques were used in the individual layers of the hadronic calorimeters to show that the background from neutrals is negligible in those layers [5].

The distribution of this background estimate is shown in Figure 5 for data and simulation with the two different physics lists. The contribution from neutral particles falls from 0.1 at low momentum to around 0.03 for particles above 7 GeV. Although the simulation captures the overall trend, it significantly overestimates the neutral contribution for tracks with momentum between 2 and 8 GeV. This effect was also seen in the tails of the  $E/p$  distributions in Figure 3.

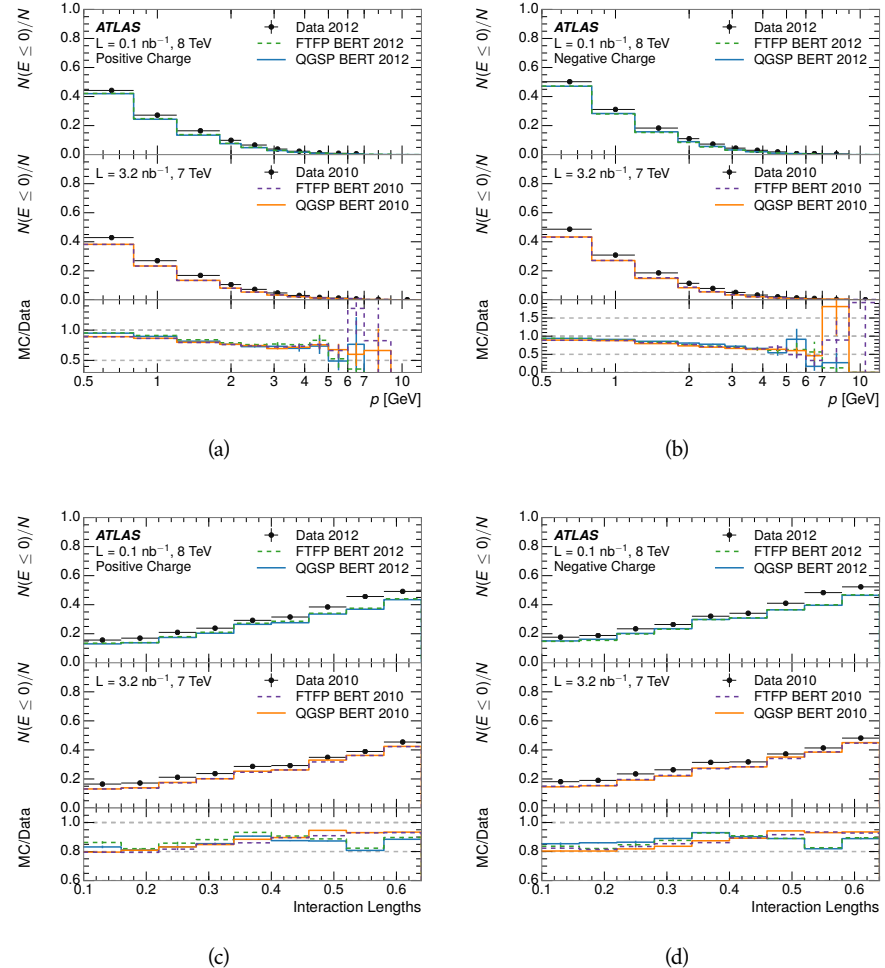


Figure 4: The fraction of tracks as a function (a, b) of momentum, (c, d) of interaction lengths with  $E \leq 0$  for tracks with positive (on the left) and negative (on the right) charge.

609 This difference is likely due to modeling of coherent neutral particle radiation  
 610 in Pythia8 that overestimates the production of  $\pi^0$  near the production of the  
 611 charged particles. The discrepancy does not depend on  $\eta$  and thus is unlikely to  
 612 be a mismodeling of the detector. This difference can be subtracted to form a  
 613 corrected average  $E/p$ , as in Section 8.2.4.

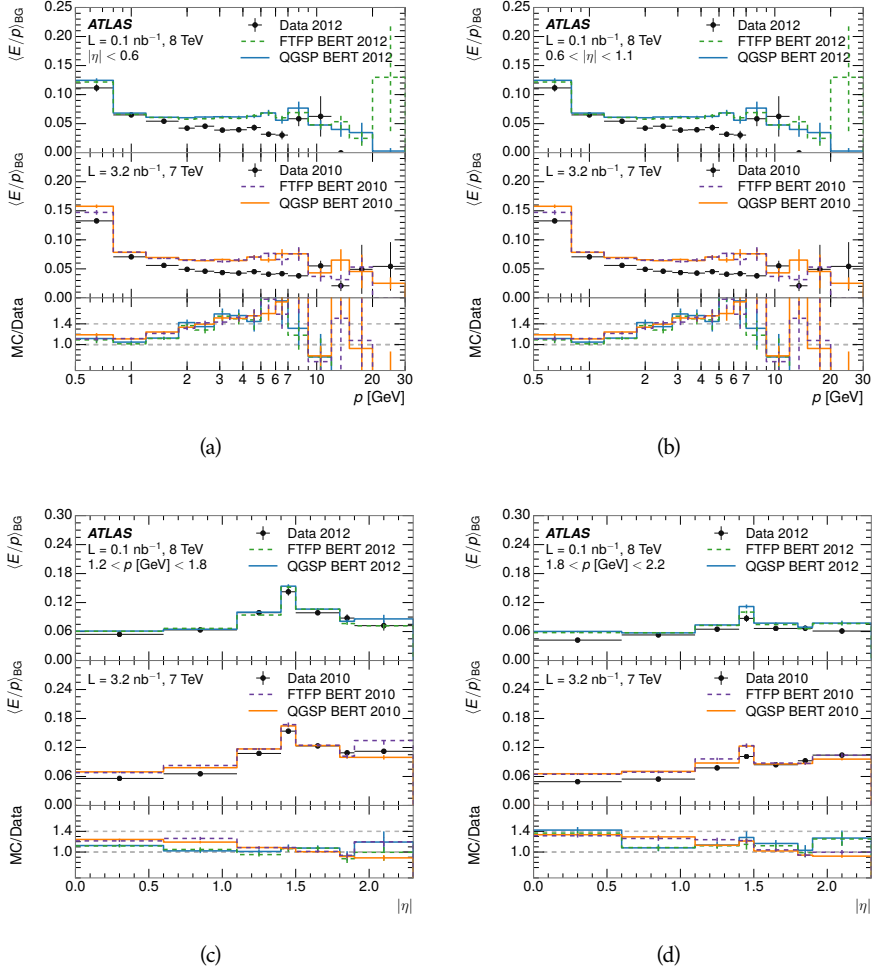


Figure 5:  $\langle E/p \rangle_{\text{BG}}$  as a function of the track momentum for tracks with (a)  $|\eta| < 0.6$ , (b)  $0.6 < |\eta| < 1.1$ , and as a function of the track pseudorapidity for tracks with (c)  $1.2 < p/\text{GeV} < 1.8$ , (d)  $1.8 < p/\text{GeV} < 2.2$ .

#### 614 8.2.4 CORRECTED RESPONSE

615 Figure 6 shows  $\langle E/p \rangle_{\text{COR}}$  as a function of momentum for several bins of pseudo-  
 616 rapidity. This corrected  $\langle E/p \rangle_{\text{COR}} \equiv \langle E/p \rangle - \langle E/p \rangle_{\text{BG}}$  measures the average  
 617 calorimeter response without the contamination of neutral particles. It is the  
 618 most direct measurement of calorimeter response in that it is the energy mea-  
 619 sured for fully isolated hadrons. The correction is performed separately in data  
 620 and simulation, so that the mismodeling of the neutral background in simulation  
 621 is removed from the comparison of response. The simulation overestimates the

622 response at low momentum by about 5%, an effect that can be mostly attributed  
 623 to the underestimation of the zero fraction mentioned previously. For  $|\eta| < 0.6$ ,  
 624 the data-simulation agreement has a larger discrepancy by about 5% for 2010  
 625 than 2012, although this is not reproduced in at higher pseudorapidity.

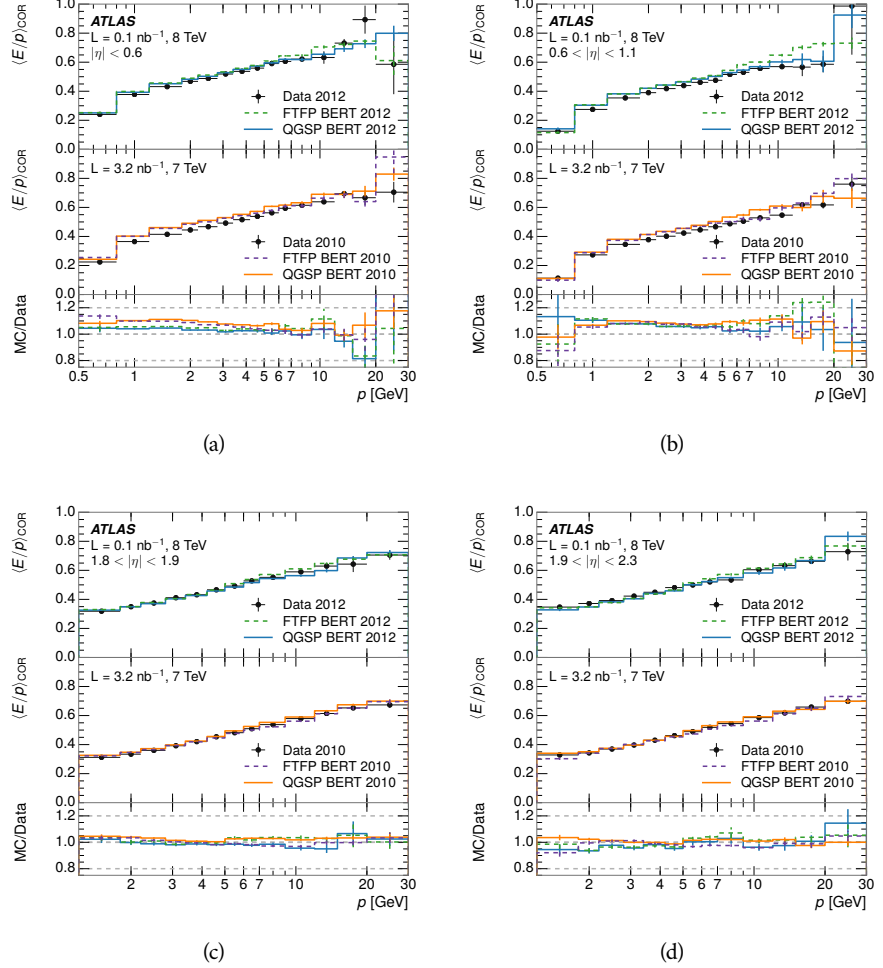


Figure 6:  $\langle E/p \rangle_{\text{COR}}$  as a function of track momentum, for tracks with (a)  $|\eta| < 0.6$ , (b)  $0.6 < |\eta| < 1.1$ , (c)  $1.8 < |\eta| < 1.9$ , and (d)  $1.9 < |\eta| < 2.3$ .

626 The response measurement above used topological clustering at the EM scale,  
 627 that is clusters were formed to measure energy but no corrections were applied  
 628 to correct for expected effects like energy lost outside of the cluster or in unin-  
 629 strumented material. It is also interesting to measure  $\langle E/p \rangle_{\text{COR}}$  using local clus-  
 630 ter weighted ([LCW](#)) energies, which accounts for those effects by calibrating the  
 631 energy based on the properties of the cluster such as energy density and depth in  
 632 the calorimeter. Figure 7 shows these distributions for tracks with zero or more  
 633 clusters and separately for tracks with one or more clusters. The calibration  
 634 moves the mean value of  $\langle E/p \rangle_{\text{COR}}$  significantly closer to 1.0 as desired. The  
 635 agreement between data and simulation improves noticeably when at least one  
 636 cluster is required, as this removes the contribution from the mismodeling of  
 637 the zero fraction. The good agreement in that case again demonstrates that the

difference in  $\langle E/p \rangle_{\text{COR}}$  between data and simulation is caused predominantly by the difference in zero fraction.

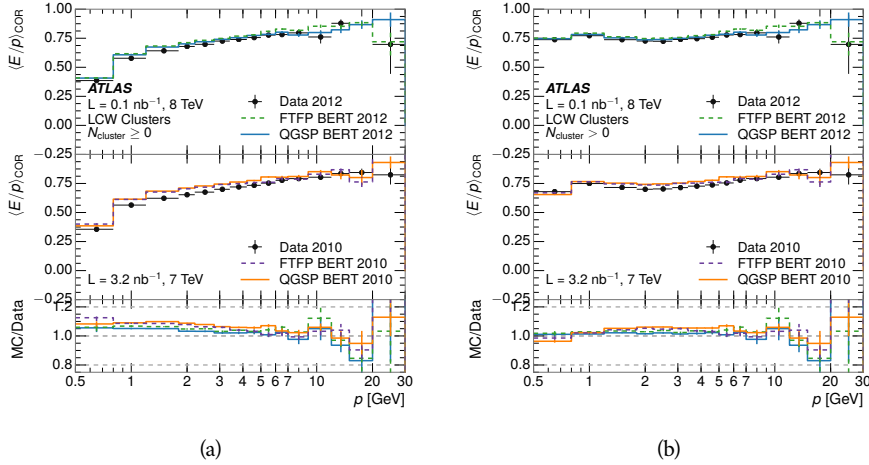


Figure 7:  $\langle E/p \rangle_{\text{COR}}$  calculated using LCW-calibrated topological clusters as a function of track momentum for tracks with (a) zero or more associated topological clusters or (b) one or more associated topological clusters.

#### 8.2.5 ADDITIONAL STUDIES

As has been seen in several measurements in previous sections, the simulation does not correctly model the chance of a low momentum hadron to reach the calorimeter. Because of the consistent discrepancy across pseudorapidity and interaction lengths, this can be best explained by incomplete understanding of hadronic interactions with the detector [4]. For example, a hadron that scatters off of a nucleus in the inner detector can be deflected through a significant angle and not reach the expected location in the calorimeter. In addition, these interactions can produce secondary particles that are difficult to model.

The requirement used throughout the previous sections on the number of hits in the TRT reduces these effects by preferentially selecting tracks that do not undergo nuclear interactions. It is interesting to check how well the simulation models tracks with low numbers of TRT hits, which selects tracks that are more likely to have undergone a hadronic interaction. Figure 8 compares the distributions with  $N_{\text{TRT}} < 20$  to  $N_{\text{TRT}} > 20$  for real and simulated particles. As expected, the tracks with fewer hits are poorly modeled in the simulation as  $\langle E/p \rangle_{\text{COR}}$  differs by as much as 25% at low momentum.

Another interesting aspect of the simulation is the description of antiprotons at low momentum, where QGSP\_BERT and FTFP\_BERT have significant differences. This can be seen to have an effect in the inclusive response measurement when separated into positive and negative charge. The  $\langle E/p \rangle_{\text{COR}}$  distributions for positive and negative particles are shown in Figure 9, where a small difference between QGSP\_BERT and FTFP\_BERT can be seen in the distribution for negative tracks. This is demonstrated more clearly in Figure 10, which shows

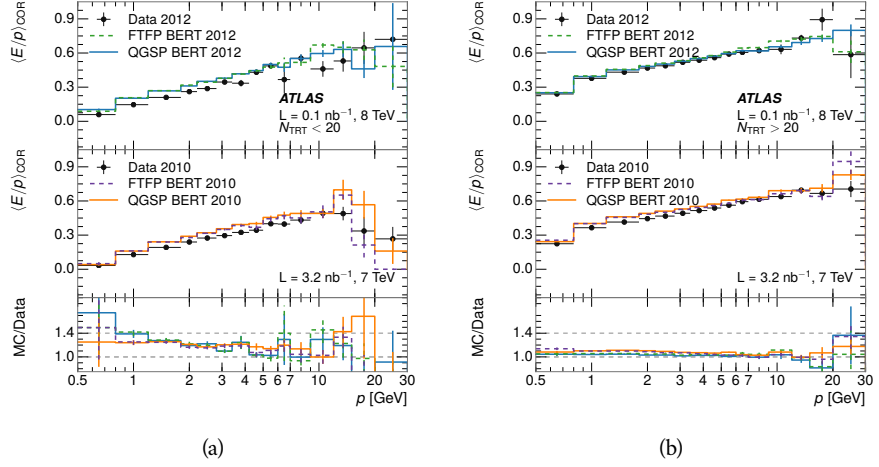


Figure 8: Comparison of the  $\langle E/p \rangle_{\text{COR}}$  for tracks with (a) less than and (b) greater than 20 hits in the TRT.

the  $E/p$  distribution in the two simulations separated by charge. There is a clear difference around  $E/p > 1.0$ , which can be explained by the additional energy deposited by the annihilation of the antiproton in the calorimeter that is modeled well only in FTFP\_BERT. This is also explored with data using identified antiprotons in Section 8.3.

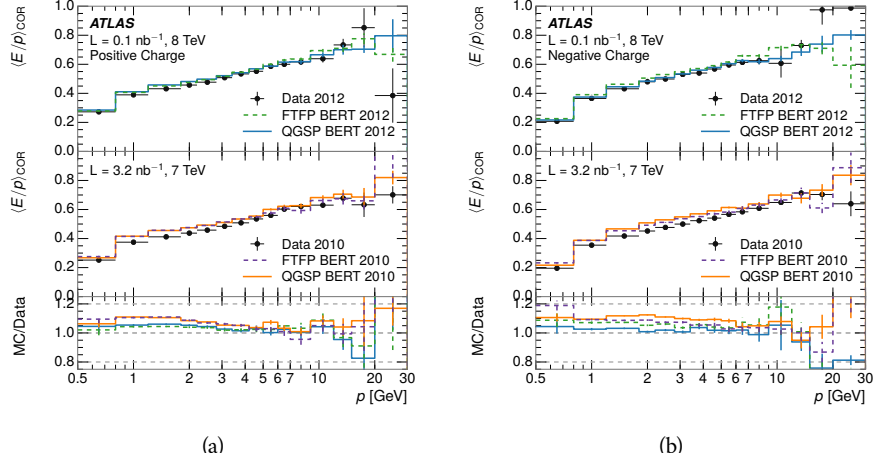


Figure 9: Comparison of the  $\langle E/p \rangle_{\text{COR}}$  for (a) positive and (b) negative tracks as a function of track momentum for tracks with  $|\eta| < 0.6$ .

The  $\langle E/p \rangle$  results in previous sections have considered the electromagnetic and hadronic calorimeters together as a single energy measurement, to emphasize the total energy deposited for a given particle. However, the deposits in each calorimeter are available separately and  $\langle E/p \rangle$  can be constructed for each layer. As the layers are composed of different materials and are modeled separately in the detector geometry, confirmation that the simulation matches the data well

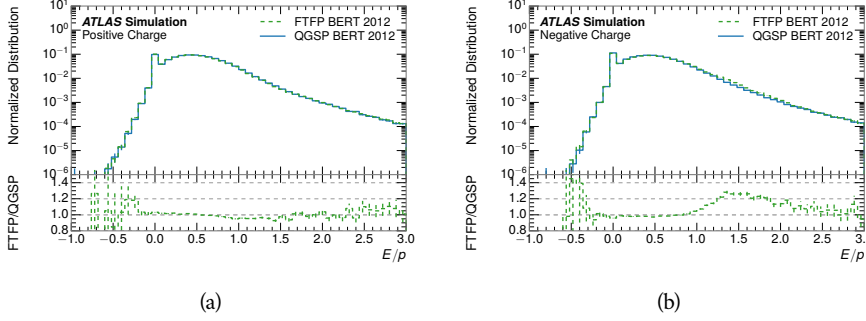


Figure 10: Comparison of the  $E/p$  distributions for (a) positive and (b) negative tracks with  $0.8 < p/\text{GeV} < 1.2$  and  $|\eta| < 0.6$ , in simulation with the FTFP\_BERT and QGSP\_BERT physics lists.

in each layer adds confidence in both the description of hadronic interactions with the two different materials and also the geometric description of each.

The technique discussed in Section 8.2.3 for selecting minimally ionizing particle (MIP)s in the electromagnetic calorimeter is also useful in studying deposits in the hadronic calorimeter. Those MIPs deposit almost all of their energy exclusively in the hadronic calorimeter. Figure 11 shows  $\langle E/p \rangle_{\text{RAW}}^{\text{Had}}$ , where RAW indicates that no correction has been applied for neutral backgrounds and Had indicates that only clusters for the hadronic calorimeter are included. The RAW and COR versions of  $\langle E/p \rangle$  in this case are the same, as the neutral background is negligible in that calorimeter layer. The distributions are shown both for the original EM scale calibration and after LCW calibration. The data and simulation agree very well in this comparison, except in the lowest momentum bin which has 5% discrepancy that has already been seen in similar measurements.

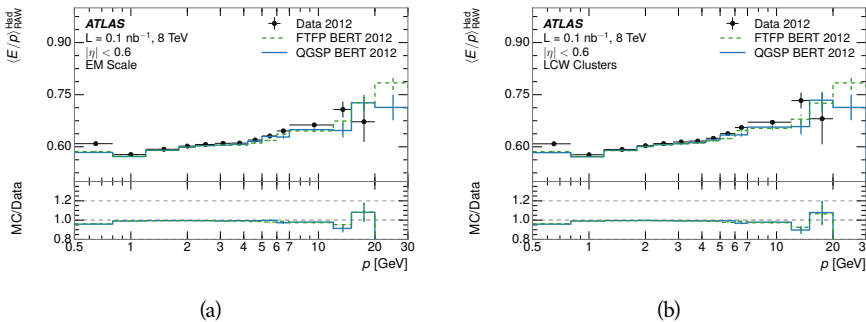


Figure 11: Comparison of the response of the hadronic calorimeter as a function of track momentum (a) at the EM-scale and (b) after the LCW calibration.

A similar comparison can be made in the electromagnetic calorimeter by selecting particles which have no associated energy in the hadronic calorimeter. These results are measured in terms of  $\langle E/p \rangle_{\text{COR}}^{\text{EM}}$ , where EM designates that only clusters in the electromagnetic calorimeter are included and COR designates that the neutral background is subtracted as the neutral background is present in this case. Figure 12 shows the analogous comparisons to Figure 11 in

694 the electromagnetic calorimeter. In this case the disagreement between data and  
 695 simulation is more pronounced, with discrepancies as high as 5% over a larger  
 696 range of momenta. This level of discrepancy indicates that the description of  
 697 the electromagnetic calorimeter is actually the dominant source of discrepancy  
 698 in the combined distributions in Section 8.2.4.

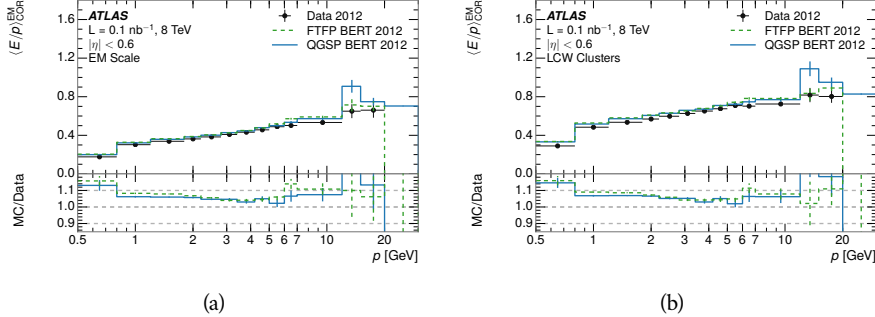


Figure 12: Comparison of the response of the EM calorimeter as a function of track momentum (a) at the EM-scale and (b) with the LCW calibration.

699 **NOTE: There are more studies that I skipped for brevity that could be in-**  
 700 **cluded if interesting.  $E/p$  at different cluster threshold settings,  $E/p$  with**  
 701 **pileup,  $E/p$  with cells. I also left out a lot of eta bins that appear in the**  
 702 **paper so that this section didn't turn into 20 pages of plots.**

### 703 8.3 IDENTIFIED PARTICLE RESPONSE

704 The inclusive response measurement for hadrons can be augmented by measur-  
 705 ing the response for specific particle species. The simulation models each parti-  
 706 cle type separately, and understanding the properties of each is important in con-  
 707 straining the uncertainty on jets. In order to select and measure specific hadrons,  
 708 this section relies on the displaced decays of long-lived particles. Such decays  
 709 can be identified by reconstructing secondary vertices with a requirement on  
 710 mass. In particular,  $\Lambda$ ,  $\bar{\Lambda}$ , and  $K_S^0$  can be used to select a pure sample of protons,  
 711 antiprotons, and pions, respectively.

#### 712 8.3.1 DECAY RECONSTRUCTION

713 The measurement of response for identified particles uses the same selection as  
 714 for inclusive particles (Section 8.1.3) with a few additions. Each event used is  
 715 required to have at least one secondary vertex, and the tracks are required to  
 716 match to that vertex rather than the primary vertex. Pions are selected from  
 717 decays of  $K_S^0 \rightarrow \pi^+ \pi^-$ , which is the dominant decay for  $K_S^0$  to charged particles.  
 718 Protons are selected from decays of  $\Lambda \rightarrow \pi^- p$  and antiprotons from  $\bar{\Lambda} \rightarrow \pi^+ \bar{p}$ ,  
 719 which are similarly the dominant decays of  $\Lambda$  and  $\bar{\Lambda}$  to charged particles. The  
 720 species of parent hadron in these decays is determined by reconstructing the  
 721 mass of the tracks associated to the secondary vertex. The sign of the higher

722 momentum decay particle can distinguish between  $\Lambda$  and  $\bar{\Lambda}$ , which of course  
 723 have the same mass, as the proton or antiproton is kinematically favored to have  
 724 higher momentum. Examples of the reconstructed masses used to select these  
 725 decays are shown in Figure 13.

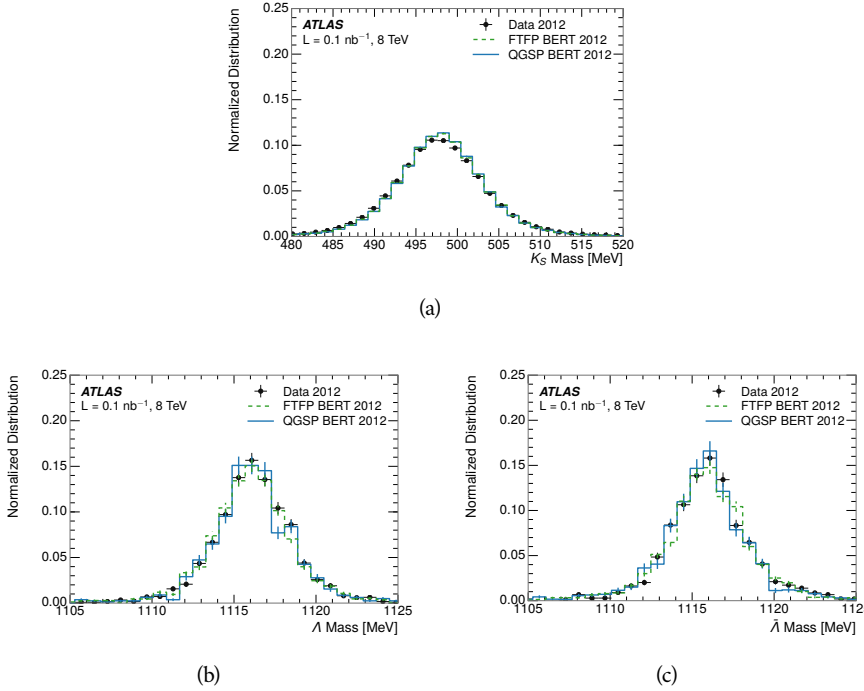


Figure 13: The reconstructed mass peaks of (a)  $K_S^0$ , (b)  $\Lambda$ , and (c)  $\bar{\Lambda}$  candidates.

726 The dominant backgrounds for the identified particle decays are nuclear in-  
 727 teractions and combinatoric sources. These are suppressed by the kinematic re-  
 728 quirements on the tracks as well as an additional veto which removes candidates  
 729 that are consistent with both a  $\Lambda$  or  $\bar{\Lambda}$  and a  $K_S^0$  hypothesis, which is possible be-  
 730 cause of the different assumptions on particle mass in each case [5]. After these  
 731 requirements, the backgrounds are found to be negligible compared to the sta-  
 732 tistical errors on these measurements.

### 733 8.3.2 IDENTIFIED RESPONSE

734 With these techniques the  $E/p$  distributions are extracted in data and simulation  
 735 for each particle species and shown in Figure 14. These distributions are shown  
 736 for a particular bin of  $E_a$  ( $2.2 < E_a/\text{GeV} < 2.8$ ), rather than  $p$ .  $E_a$  is the energy  
 737 available to be deposited in the calorimeter: for pions  $E_a = \sqrt{p^2 + m^2}$ , for pro-  
 738 tons  $E_a = \sqrt{p^2 + m^2} - m$ , and for antiprotons  $E_a = \sqrt{p^2 + m^2} + m$ . The features  
 739 of the  $E/p$  distributions are similar to the inclusive case. There is a small nega-  
 740 tive tail from noise and a large fraction of tracks with zero energy from particles  
 741 which do not reach the calorimeter. The long positive tail is noticeably more  
 742 pronounced for antiprotons because of the additional energy generated by the  
 743 annihilation in addition to the neutral background.

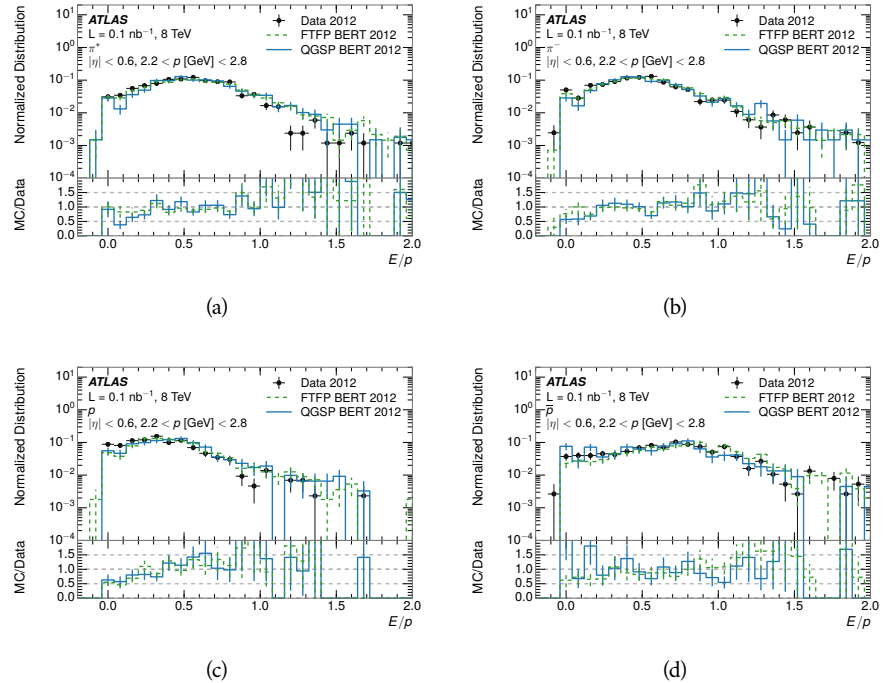


Figure 14: The  $E/p$  distribution for isolated (a)  $\pi^+$ , (b)  $\pi^-$ , (c) proton, and (d) anti-proton tracks.

The zero fraction is further explored in Figure 15 for pions and protons in data and simulation. The simulation consistently underestimates the zero fraction independent of particle species, which implies that this discrepancy is not caused by the model of a particular species but rather a feature common to all.

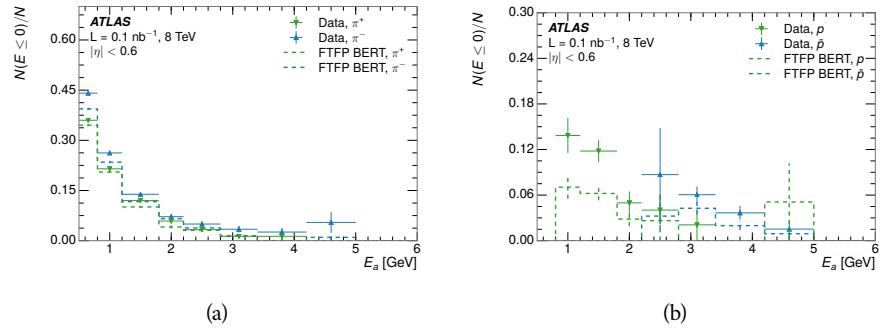


Figure 15: The fraction of tracks with  $E \leq 0$  for identified (a)  $\pi^+$  and  $\pi^-$ , and (b) proton and anti-proton tracks

It is also interesting to compare the response between the different particle species. One approach to do this is to measure the difference in  $\langle E/p \rangle$  between two types, which has the advantage of removing the neutral background. These differences are shown in various combinations in Figure 16. The response for  $\pi^+$  is greater on average than the response to  $\pi^-$  because of a charge-exchange effect which causes the production of additional neutral pions in the showers of

754  $\pi^+$  [27]. The response for  $\pi^+$  is also greater on average than the response to  $p$ ,  
 755 because a large fraction of the energy of  $\pi^+$  hadrons is converted to an electro-  
 756 magnetic shower [28, 29]. However, the  $\bar{p}$  response is significantly higher than  
 757 the response to  $\pi^-$  because of the annihilation of the antiproton. FTFP\_BERT  
 758 does a better job of modeling this effect than QGSP\_BERT because of their differ-  
 759 ent descriptions of  $\bar{p}$  interactions with material.

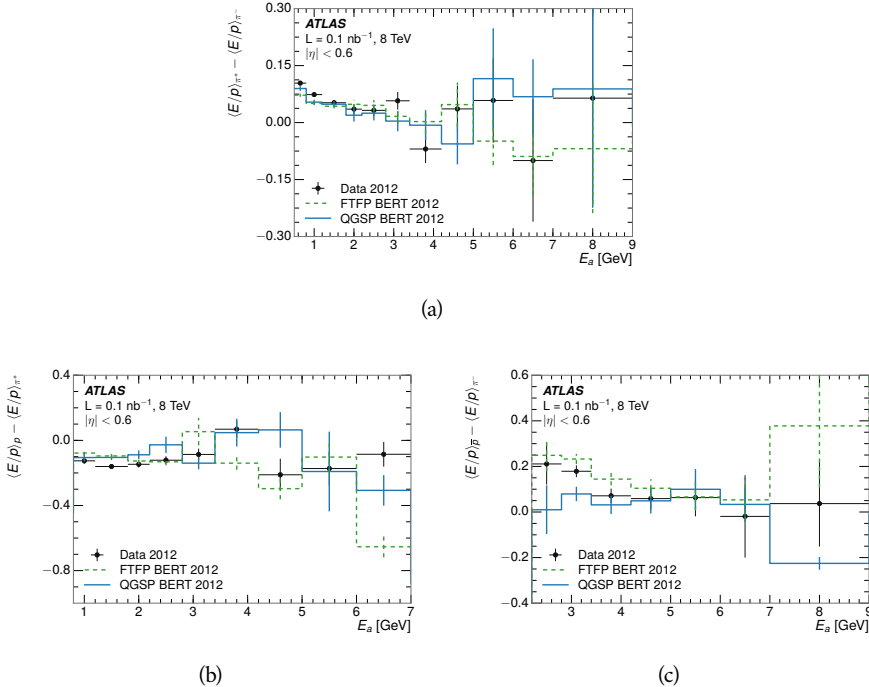


Figure 16: The difference in  $\langle E/p \rangle$  between (a)  $\pi^+$  and  $\pi^-$  (b)  $p$  and  $\pi^+$ , and (c)  $\bar{p}$  and  $\pi^-$ .

760 It is also possible to remove the neutral background from these response dis-  
 761 tributions using the same technique as in Section 8.2.3. The technique is largely  
 762 independent of the particle species and so can be directly applied to  $\langle E/p \rangle$  for  
 763 pions. The  $\langle E/p \rangle_{\text{COR}}$  distributions for pions are shown in Figure 17, which are  
 764 very similar to the inclusive results. The inclusive hadrons are comprised mostly  
 765 of pions, so this similarity is not surprising. It is also possible to see the small  
 766 differences between  $\pi^+$  and  $\pi^-$  response here, where  $\langle E/p \rangle_{\text{COR}}$  is higher on av-  
 767 erage for  $\pi^+$ . The agreement between data and simulation is significantly worse  
 768 for the  $\pi^-$  distributions than for the  $\pi^+$ , with a discrepancy greater than 10%  
 769 below 2-3 GeV.

### 770 8.3.3 ADDITIONAL SPECIES IN SIMULATION

771 The techniques above provide a method to measure the response separately for  
 772 only pions and protons. However the hadrons which forms jets include a num-  
 773 ber of additional species such as kaons and neutrons. The charged kaons are  
 774 an important component of the inclusive charged hadron distribution, which is  
 775 comprised of roughly 60-70% pions, 15-20% kaons, and 5-15% protons. These

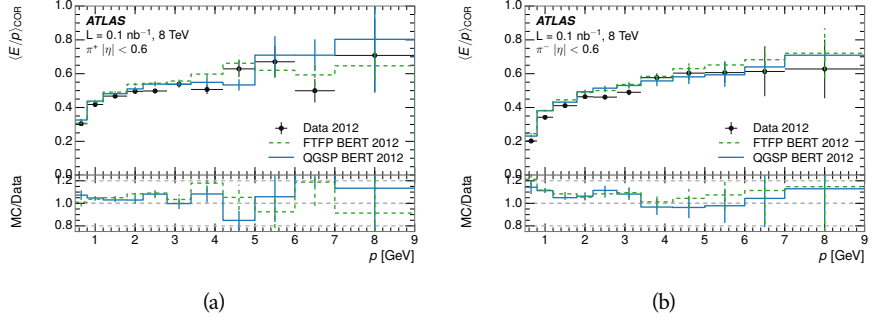


Figure 17:  $\langle E/p \rangle_{\text{COR}}$  as a function of track momentum for (a)  $\pi^+$  tracks and (b)  $\pi^-$  tracks.

are difficult to measure in data at the ATLAS detector, although a template subtraction technique has been proposed which may be effective with larger sample sizes [4]. The simulation of these particles includes noticeable differences in response at low energies, which are shown in Figure 18 for FTFP\_BERT. The significant differences in response between low energy protons and antiprotons are accounted for above in the definitions of  $E_a$ .

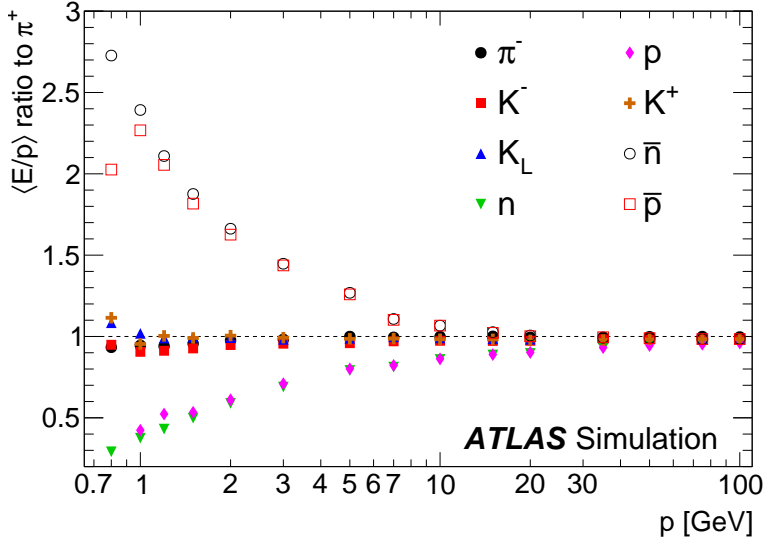


Figure 18: The ratio of the calorimeter response to single particles of various species to the calorimeter response to  $\pi^+$  with the physics list FTFP\_BERT.

#### 8.4 SUMMARY

These various measurements of calorimeter response shown above for data and simulation illuminate the accuracy of the simulation of hadronic interactions at the ATLAS detector. The results were done using 2010 and 2012 data at 7 and 8 TeV, but reflect the most current understanding of the detector alignment and geometry. A number of measurements focusing on a comparison between pro-

788 tons and antiprotons suggest that FTFP\_BERT models those interaction more  
789 accurately than QGSP\_BERT. These measurements, among others, were the moti-  
790 vation to switch the default Geant4 simulation from FTFP\_BERT to QGSP\_BERT  
791 for all ATLAS samples.

792 Even with these updates, there are a number of small, approximately 5%, dis-  
793 crepancies in response between the data and simulation at low energies. At  
794 higher energies the simulation of hadronic interactions is very consistent with  
795 data. Chapter 9 discusses how to use these observed differences to constrain the  
796 jet energy scale and its associated uncertainties.



797

798 JET ENERGY RESPONSE AND UNCERTAINTY

---

## 799 9.1 MOTIVATION

800 As jets form a major component of many physics analyses at ATLAS, it is cru-  
 801 cial to carefully calibrate the measurement of jet energies and to derive an un-  
 802 certainty on that measurement. These uncertainties have often been the dom-  
 803 inant systematic uncertainty in high-energy analyses at the Large Hadron Col-  
 804 lide (LHC). Dijet and multijet balance techniques provide a method to constrain  
 805 the JES and its uncertainty in data, and provide the default values used for ATLAS  
 806 jet measurements at most energies [30]. These techniques are limited by their re-  
 807 liance on measuring jets in data, so they are statistically limited in estimating  
 808 the jet energy scale at the highest jet energies. This chapter presents another  
 809 method for estimating the jet energy scale and its uncertainty which builds up a  
 810 jet from its components and thus can be naturally extended to high jet momen-  
 811 tum. Throughout this chapter the jets studied are simulated using Pythia8 with  
 812 the CT10 parton distribution set [31] and the AU2 tune [8], and corrections are  
 813 taken from the studies including data and simulation in Chapter 8.

814 As described in Section 7.2, jets are formed from topological clusters of energy  
 815 in the calorimeters using the anti- $k_t$  algorithm. These clusters originate from a  
 816 diverse spectrum of particles, in terms of both species and momentum, leading to  
 817 significantly varied jet properties and response between jets of similar produced  
 818 momentum. Figure 19 shows the simulated distribution of particles within jets  
 819 at a few examples energies. The  $E/p$  measurements provide a thorough under-  
 820 standing of the dominant particle content of jets, the charged hadrons.

## 821 9.2 UNCERTAINTY ESTIMATE

822 Simulated jets are not necessarily expected to correctly model the energy de-  
 823 posits in the calorimeters, because of the various discrepancies discussed in Chap-  
 824 ter 8. To evaluate a jet energy response, the simulated jet energies are compared  
 825 to a corrected jet built up at the particle level. Each cluster in a jet is associated  
 826 to the truth particle which deposited it, and the energy in that cluster is then  
 827 corrected for a number of effects based on measurements in data. The primary  
 828 corrections come from the single hadron response measurements in addition  
 829 to response measured using the combined test beam which covers higher mo-  
 830 mentum particles [32]. These corrections include both a shift ( $\Delta$ ), in order to  
 831 make the simulation match the average response in data, and an uncertainty ( $\sigma$ )  
 832 associated with the ability to constrain the difference between data and simula-  
 833 tion. Some of the dominant sources of uncertainty are itemized in Table 1 with  
 834 typical values, and the full list considered is described in detail in the associated

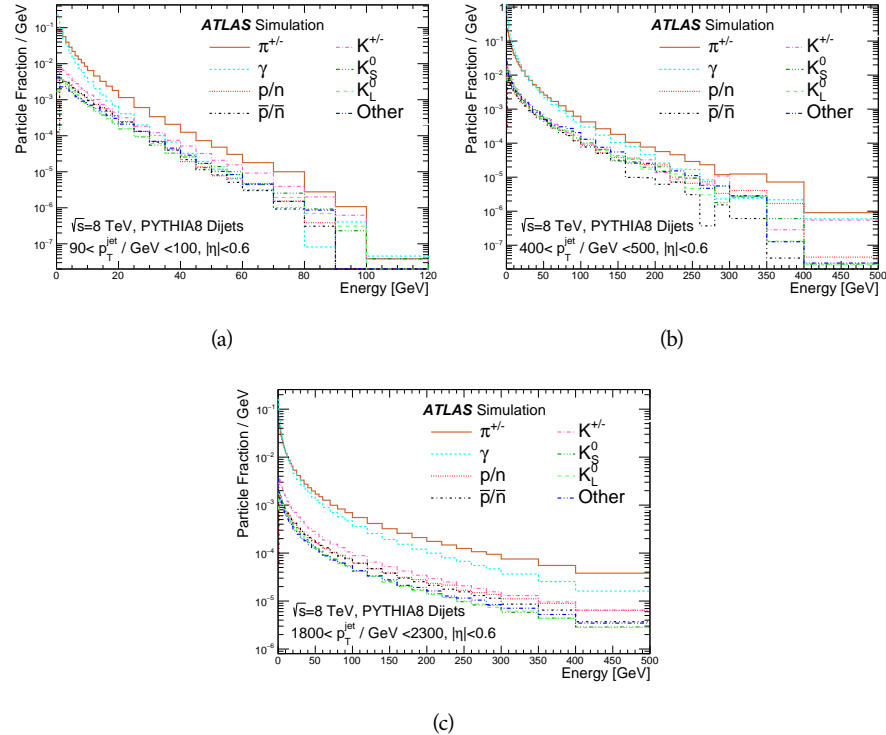


Figure 19: The spectra of true particles inside anti- $k_t$ ,  $R = 0.4$  jets with (a)  $90 < p_T/\text{GeV} < 100$ , (b)  $400 < p_T/\text{GeV} < 500$ , and (c)  $1800 < p_T/\text{GeV} < 2300$ .

paper [4]. These uncertainties cover differences between the data and simulation in the modeling of calorimeter response to a given particle. No uncertainties are added for the difference between particle composition of jets in data and simulation.

From these terms, the jet energy scale and uncertainty is built up from individual energy deposits in simulation. Each uncertainty term is treated independently, and are taken to be gaussian distributed. The resulting scale and uncertainty is shown in Figure 20, where the mean response is measured relative to the calibrated energy reported by simulation. The dominant uncertainties come from the statistical uncertainties on the  $E/p$  measurements at lower energies and the additional uncertainty for out of range measurements at higher energies. The total uncertainty from this method at intermediate jet energies is comparable to other simulation-based methods [33] and is about twice as large as in-situ methods using data [30]. This method is the only one which provides an estimation above 1.8 TeV, however, and so is still a crucial technique in analyses that search for very energetic jets.

These techniques can also be used to measure the correlation between bins of average reconstructed jet momentum across a range of  $p_T$  and  $|\eta|$ , where correlations are expected because of a similarity in particle composition at similar energies. Figure 21 shows these correlations, where the uncertainties on jets in neighboring bins are typically between 30% and 60% correlated. The uncertainty on all jets becomes significantly correlated at high energies and larger pseudora-

Abbrev.	Description	$\Delta$ (%)	$\sigma$ (%)
In situ $E/p$	The comparison of $\langle E/p \rangle_{\text{COR}}$ as described in Chapter 8 with statistical uncertainties from 500 MeV to 20 GeV.	0-3	1-5
CTB	The main $\langle E/p \rangle$ comparison uncertainties, binned in $p$ and $ \eta $ , as derived from the combined test beam results, from 20 to 350 GeV [32].	0-3	1-5
$E/p$ Zero Fraction	The difference in the zero-fraction between data and MC simulation from 500 MeV to 20 GeV.	5-25	1-5
$E/p$ Threshold	The uncertainty in the EM calorimeter response from the potential mismodeling of threshold effects in topological clustering.	0	0-10
Neutral	The uncertainty in the calorimeter response to neutral hadrons based on studies of physics model variations.	0	5-10
$K_L$	An additional uncertainty in the response to neutral $K_L$ in the calorimeter based on studies of physics model variations.	0	20
$E/p$ Misalignment	The uncertainty in the $p$ measurement from misalignment of the ID.	0	1
Hadrons, $p > 350$ GeV	A flat uncertainty for all particles above the energy range or outside the longitudinal range probed with the combined test beam.	0	10

Table 1: The dominant sources of corrections and systematic uncertainties in the [JES](#) estimation technique, including typical values for the correcting shift ( $\Delta$ ) and the associated uncertainty ( $\sigma$ ).

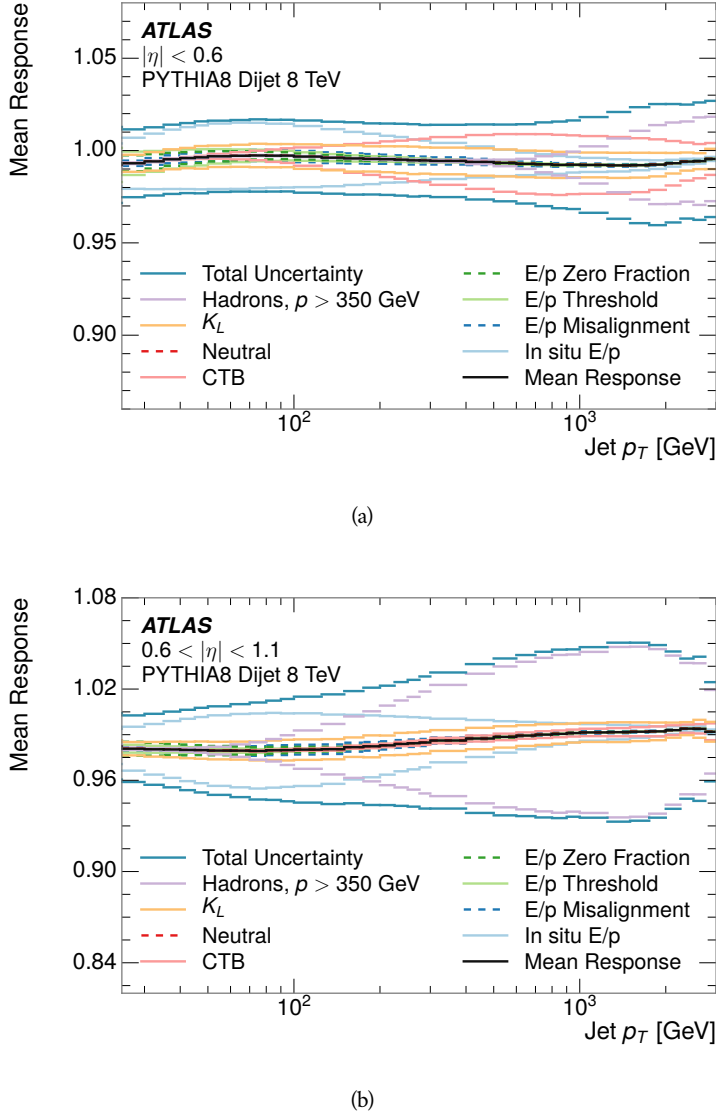


Figure 20: The [JES](#) uncertainty contributions, as well as the total [JES](#) uncertainty, as a function of jet  $p_T$  for (a)  $|\eta| < 0.6$  and (b)  $0.6 < |\eta| < 1.1$ .

857      p idities, when the uncertainty becomes dominated by the single term reflecting  
 858      out of range particles.

### 859      9.3 SUMMARY

860      The technique described above provides a jet energy scale and uncertainty by  
 861      building up jet corrections from the energy deposits of constituent particles. The  
 862       $E/p$  measurements are crucial in providing corrections for the majority of parti-  
 863      cles in the jets. The uncertainty derived this way is between 2 and 5% and is about  
 864      twice as large at corresponding momentum than jet balance methods. However  
 865      this is the only uncertainty available for very energetic jets using 2012 data and  
 866      simulation, and repeating this method with Run 2 data and simulation will be

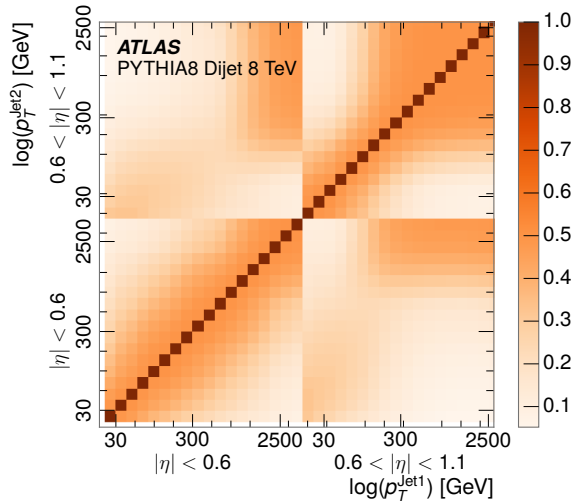


Figure 21: The JES correlations as a function of jet  $p_T$  and  $|\eta|$  for jets in the central region of the detector.

867 important in providing an uncertainty for the most energetic jets in 13 TeV col-  
 868 lisions.



869

## PART V

870

### SEARCH FOR LONG-LIVED PARTICLES

871

You can put some informational part preamble text here.



874 As discussed in Section 2.3, various limitations in the SM suggest a need for new  
 875 particles at the TeV scale. A wide range of extensions to the Standard Model  
 876 predict that these new particles can have lifetimes greater than approximately  
 877 one-hundredth of a nanosecond. These include theories with universal extra-  
 878 dimensions [34, 35], with new fermions [36], and with leptoquarks [37]. Many  
 879 Supersymmetry (SUSY) theories also produce these Long-Lived Particles (LLPs),  
 880 in both R-Parity violating [38–40] and R-Parity conserving [41–44] formula-  
 881 tions. Split supersymmetry [45, 46], for example, predicts long-lived gluinos  
 882 with  $O(\text{TeV})$  masses. This search focuses specifically on the SUSY case, but many  
 883 of the results are generic to any model with LLPs.

884 Long-lived gluinos or squarks carry color-charge and will thus hadronize into  
 885 color neutral bound states called R-Hadrons. These are composit particles like  
 886 the usual hadrons but with one supersymmetric constituent, for example  $\tilde{g}q\bar{q}$   
 887 and  $\tilde{q}\bar{q}$ . Through this hadronization process, the neutral gluino can acquire a  
 888 charge. Gluino pair production,  $pp \rightarrow \tilde{g}\tilde{g}$  has the largest cross sectional increase  
 889 with the increase in energy to 13 TeV, and so this search focuses on gluino R-  
 890 Hadrons. Planned future updates will extend the case to explicitly include squark  
 891 and chargino models, but the method covers any long-lived, charged, massive  
 892 particle.

## 893 10.1 EVENT TOPOLOGY

894 The majority of SUSY models predict that gluinos will be produced in pairs at  
 895 the LHC, through processes like  $pp \rightarrow q\bar{q} \rightarrow \tilde{g}\tilde{g}$  and  $pp \rightarrow gg \rightarrow \tilde{g}\tilde{g}$ , where the  
 896 gluon mode dominates for the collision energy and gluino masses considered  
 897 for this search. During their production, the long-lived gluinos hadronize into  
 898 color singlet bound states including  $\tilde{g}q\bar{q}$ ,  $\tilde{g}qqq$ , and even  $\tilde{g}g$  [47]. The probability  
 899 to form the gluon-only bound states is a free parameter usually taken to be 0.1,  
 900 while the meson states are favored among the R-Hadrons [48]. The charged and  
 901 neutral states are approximately equally likely for mesons, so the R-Hadrons will  
 902 be charged roughly 50% of the time.

903 These channels produce R-Hadrons with large  $p_T$ , comparable to their mass,  
 904 so that they typically propagate with  $0.2 < \beta < 0.9$  [48]. The fragmentation that  
 905 produces these hadrons is very hard, so the jet structure around the R-Hadron  
 906 is minimal, with less than 5 GeV of summed particle momentum expected in a  
 907 cone of  $\Delta R < 0.25$  around the R-Hadron [48]. After hadronization, depending  
 908 on the gluino lifetime, the R-Hadrons then decay into hadrons and a LSP [47].

909 In summary, the expected event for pair-produced long-lived gluinos is very  
 910 simple: two isolated, high-momentum R-Hadrons that propagate through the  
 911 detector before decaying into jets. The observable features of such events depend

912 strongly on the interaction of the R-Hadron with the material of the detector and  
 913 also its lifetime. Section 10.1.1 describes the interactions of R-Hadrons which  
 914 reach the various detector elements in A Toroidal LHC ApparatuS ([ATLAS](#)) and  
 915 Section 10.1.2 provides a summary of the observable event descriptions for R-  
 916 Hadrons of various lifetimes.

917 10.1.1 DETECTOR INTERACTIONS

918 After approximately 0.2 ns, the R-Hadron reaches the pixel detector. If charged,  
 919 it deposits energy into the material through repeated single collisions that result  
 920 in ionization of the silicon substrate [49]. Because of its comparatively low  $\beta$ ,  
 921 the ionization energy can be significantly greater than expected for SM particles  
 922 because the most-probable energy loss grows significantly as  $\beta$  decreases [49].  
 923 This large ionization can be measured through the time over threshold (ToT) read  
 924 out from the pixel detector as described in Section 7.1.1.2. Large ionization in  
 925 the inner detector is one of the major characteristic features of LLPs.

926 Throughout the next few nanoseconds, the R-Hadron propagates through the  
 927 remainder of the inner detector. A charged R-Hadron will provide hits in each  
 928 of these systems as would any other charged particle, and can be reconstructed  
 929 as a track. The track reconstruction provides a measurement of its trajectory  
 930 and thus its momentum as described in Section 7.1. The large momentum is  
 931 another characteristic feature of massive particles produced at the LHC. **Note: At**  
 932 **this point I am failing to mention that the TRT provides a possible dE/dx**  
 933 **measurement, because no one uses it as far as I know.**

934 As of roughly 20 ns, the R-Hadron enters the calorimeter where it interacts  
 935 hadronically with the material. Because of its large mass and momentum, the  
 936 R-Hadron does not typically stop in the calorimeter, but rather deposits a small  
 937 fraction of its energy through repeated interactions with nucleons. The proba-  
 938 bility of interaction between the gluino itself and a nucleon is low because the  
 939 cross section drops off with the inverse square of its mass, so the interactions are  
 940 primarily governed by the light constituents [50]. Each of these interactions can  
 941 potentially change that quark content and thus change the sign of the R-Hadron,  
 942 so that the charge at exit is typically uncorrelated with the charge at entry [48].  
 943 The total energy deposited in the calorimeters during the propagation is small  
 944 compared to the kinetic energy of the R-Hadron, around 20-40 GeV, so that  
 945  $E/p$  is typically less than 0.1 [48].

946 Then, 30 ns after the collision, it reaches the muon system, where it again  
 947 ionizes in the material if charged and can be reconstructed as a muon track. Be-  
 948 cause of the charge-flipping interactions in the calorimeter, this track may have  
 949 the opposite sign of the track reconstructed in the inner detector, or there may  
 950 be a track present when there was none in the inner detector and vice-versa. The  
 951 propagation time at the typically lower  $\beta$  results in a significant delay compared  
 952 to muons, and that delay can be assessed in terms of a time-of-flight measure-  
 953 ment. Because of the probability of charge-flip and late arrival, there is a signif-  
 954 icant chance that an R-Hadron which was produced with a charge will not be

955 identified as a muon. The long time-of-flight is another characteristic feature of  
 956 R-Hadrons which are reconstructed as muons.

957 10.1.2 LIFETIME DEPENDENCE

958 The above description assumed a lifetime long enough for the R-Hadron to exit  
 959 the detector, which through this search is referred to as “stable”, even though  
 960 the particle may decay after exiting the detector. There are several unique sig-  
 961 natures at shorter lifetimes where the R-Hadron decays in various parts of the  
 962 inner detector; these lifetimes are referred to as “metastable”.

963 The shortest case where the R-Hadron is considered metastable is for life-  
 964 times around 0.01 ns, where the particle decays before reaching any of the de-  
 965 tector elements. Although the R-Hadrons are produced opposite each other in  
 966 the transverse plane, each R-Hadron decays to a jet and an [LSP](#). The [LSPs](#) are not  
 967 measured, so the produced jets can be significantly imbalanced in the transverse  
 968 plane which results in large missing energy. That missing energy can be used  
 969 to trigger candidate events, and provides the most efficient trigger option for  
 970 shorter lifetimes. Additionally, the precision of the tracking system allows the  
 971 displaced vertex of the R-Hadron decay to be reconstructed from the charged  
 972 particles in the jet. The distance of that vertex from the interaction point can  
 973 be used to distinguish R-Hadron decays from other processes. Figure 22 shows  
 974 a schematic diagram of an example R-Hadron event with such a lifetime. The  
 975 diagram is not to scale, but instead illustrates the detector interactions in the  
 976 pixel detector, calorimeters, and muon system. It includes a representation of  
 977 the charged R-Hadron and the neutral R-Hadron, as well as the [LSPs](#) and jets  
 978 (shown as charged hadrons) produced in the decay. Neutral hadrons may also  
 979 be produced in the decay but are not depicted. Previous searches on [ATLAS](#) have  
 980 used the displaced vertex to target [LLP](#) decays [51].

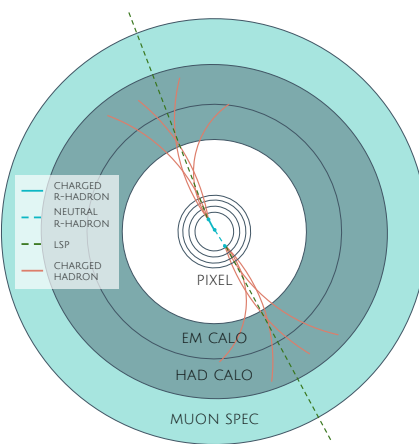


Figure 22: A schematic diagram of an R-Hadron event with a lifetime around 0.01 ns.  
 The diagram includes one charged R-Hadron (solid blue), one neutral R-  
 Hadron (dashed blue), [LSPs](#) (dashed green) and charged hadrons (solid orange).  
 The pixel detector, calorimeters, and muon system are illustrated but not to  
 scale.

981     The next distinguishable case occurs at lifetimes greater than 0.1 ns, where  
 982     the R-Hadron forms a partial track in the inner detector. If the decay products  
 983     are sufficiently soft, they may not be reconstructed, and this forms a unique sig-  
 984     nature of a disappearing track. An example of such an event is illustrated in  
 985     Figure 23, which shows the short track in the inner detector and the undetected  
 986     soft charged hadron and LSP that are produced. A dedicated search on ATLAS used  
 987     the disappearing track signature to search for LLP in Run 1 [52]. **zNote: might**  
 988     **not be worth mentioning the disappearing track here since it is actually a**  
 989     **chargino search, the soft pion is pretty unique to charginos.**

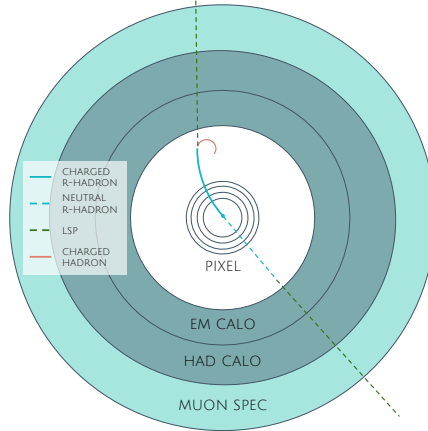


Figure 23: A schematic diagram of an R-Hadron event with a lifetime around 4 ns. The diagram includes one charged R-Hadron (solid blue), one neutral R-Hadron (dashed blue), LSPs (dashed green) and a charged hadron (solid orange). The pixel detector, calorimeters, and muon system are illustrated but not to scale.

990     If the decay products are not soft, the R-Hadron daughters form jets, resulting  
 991     in an event-level signature of up to two high-momentum tracks, jets, and signif-  
 992     icant missing energy. The missing energy has the same origin as in the case of  
 993     0.01 ns lifetimes, from the decay to unmeasured particles, and again can be large.  
 994     The high-momentum tracks will also have the characteristically high-ionization  
 995     of massive, long-lived particles in the inner detector. Figure 24 illustrates an ex-  
 996     ample event with one charged R-Hadron which decays after approximately 10 ns,  
 997     and shows how the jets from the decay can still be reconstructed in the calorime-  
 998     ter. Several previous searches on ATLAS from Run 1 have used this signature to  
 999     search for R-Hadrons [53, 54], including a dedicated search for metastable parti-  
 1000     cles [55].

1001     If the lifetime is longer than several nanoseconds, in the range of 15-30 ns,  
 1002     the R-Hadron decay can occur in or after the calorimeters, but prior to reaching  
 1003     the muon system. This case is similar to the above, although the jets may not be  
 1004     reconstructed, and is covered by many of the same search strategies. The events  
 1005     still often have large missing energy, although it is generated through different  
 1006     mechanisms. The R-Hadrons do not deposit much energy in the calorimeters, so  
 1007     a neutral R-Hadron will not enter into the missing energy calculation. A charged  
 1008     R-Hadron opposite a neutral R-Hadron will thus generate significant missing en-  
 1009     ergy, and close to 50% of pair-produced R-Hadron events fall into this category.

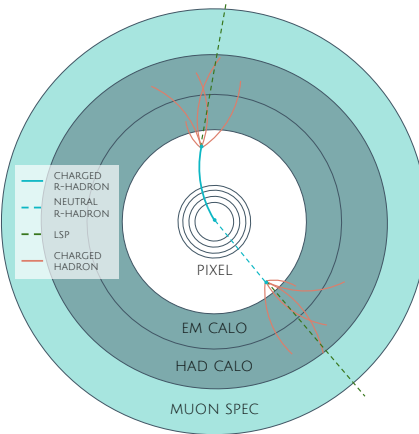


Figure 24: A schematic diagram of an R-Hadron event with a lifetime around 5 ns. The diagram includes one charged R-Hadron (solid blue), one neutral R-Hadron (dashed blue), LSPs (dashed green) and charged hadrons (solid orange). The pixel detector, calorimeters, and muon system are illustrated but not to scale.

1010 If both R-Hadrons are neutral then the missing energy will be low because nei-  
 1011 ther is detected. Two charged R-Hadrons will also result in low missing energy  
 1012 because both are reconstructed as tracks and will balance each other in the trans-  
 1013 verse plane. A small fraction of the time, one of the charged R-Hadron tracks may  
 1014 fail quality requirements and thus be excluded from the missing energy calcula-  
 1015 tion and again result in significant missing energy. Figure 25 illustrates another  
 1016 example event with one charged R-Hadron which decays after approximately 20  
 1017 ns, and shows how the jets from the decay might not be reconstructed.

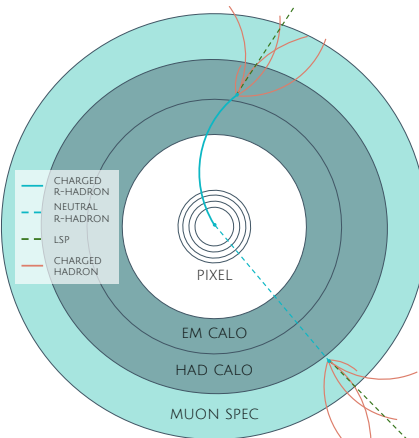


Figure 25: A schematic diagram of an R-Hadron event with a lifetime around 20 ns. The diagram includes one charged R-Hadron (solid blue), one neutral R-Hadron (dashed blue), LSPs (dashed green) and charged hadrons (solid orange). The pixel detector, calorimeters, and muon system are illustrated but not to scale.

1018 The longest lifetimes, the stable case, has all of the features of the 30-50 ns case  
 1019 but with the addition of muon tracks for any R-Hadrons that exit the calorimeter  
 1020 with a charge. That muon track can provide additional information from time-  
 1021 of-flight measurements to help identify LLPs. An example of the event topology

1022 for one charged and one neutral stable R-Hadron is shown in Figure 26. Some  
 1023 searches on [ATLAS](#) have included this information to improve the search reach  
 1024 for stable particles [54, 56].

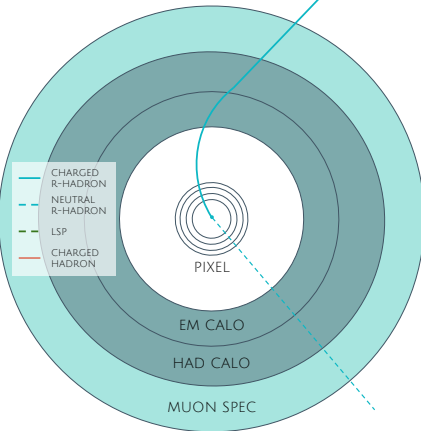


Figure 26: A schematic diagram of an R-Hadron event with a lifetime around 20 ns.  
 The diagram includes one charged R-Hadron (solid blue) and one neutral R-Hadron (dashed blue). The pixel detector, calorimeters, and muon system are illustrated but not to scale.

## 1025 10.2 SIMULATION

1026 All of the event topologies discussed above are explored by simulations of R-  
 1027 Hadron events in the [ATLAS](#) detector. A large number of such samples are gen-  
 1028 erated to determine signal efficiencies, to measure expected yields, and to esti-  
 1029 mate uncertainties. The primary interaction, pair production of gluinos with  
 1030 masses between 400 and 3000 GeV, is simulated using [Pythia 6.4.27](#) [57]  
 1031 with the AUET2B [58] set of tuned parameters for the underlying event and  
 1032 the CTEQ6L1 [31] parton distribution function ([PDF](#)) set. The simulated inter-  
 1033 actions include a modeling of pileup by adding secondary, minimum bias in-  
 1034 teractions from both the same (in-time pileup) and nearby (out-of-time pileup)  
 1035 bunch crossings. This event generation is then augmented with a dedicated  
 1036 hadronization routine to hadronize the long-lived gluinos into final states with  
 1037 R-Hadrons [59], with the probability to form a gluon-gluino bound set at 10% [60].

1038 The cross sections used for these processes are calculated at next-to-leading  
 1039 order ([NLO](#)) in the strong coupling constant with a resummation of soft-gluon  
 1040 emmision at next-to-leading logarithmic ([NLL](#)) [61–65]. The nominal predic-  
 1041 tions and the uncertainties for each mass point are taken from an envelope of  
 1042 cross-section predictions using different [PDF](#) sets and factorization and renor-  
 1043 malization scales [66].

1044 The R-Hadrons then undergo a full detector simulation [], where the interac-  
 1045 tions of the R-Hadrons with the material of the detector are described by dedi-  
 1046 cated [Geant4](#) [1] routines. These routines model the interactions described in  
 1047 Section 10.1.1, including the ionizing interactions in the silicon modules of the  
 1048 inner detector and the R-Hadron-nucleon interactions in the calorimeters [67],

1049 [68]. The specific routine chosen to describe the interactions of the R-Hadrons  
 1050 with nucleons, the “generic model”, uses a pragmatic approach where the scatter-  
 1051 ing cross section is taken to be a constant 12 mb per light quark. In this model  
 1052 the gluino itself does not interact at all except through its role as a reservoir of  
 1053 kinetic energy.

1054 The lifetimes of these R-Hadrons are then simulated at several working points,  
 1055  $\tau = 0.1, 1.0, 3.0, 10, 30, 50$  and detector stable, where the particle is required to  
 1056 decay after propagating for a time compatible with its lifetime. Only one decay  
 1057 mode is simulated for these samples,  $\tilde{g} \rightarrow q\bar{q}\tilde{\chi}_1^0$  with the neutralino mass set to  
 1058 100 GeV, which is chosen because it has the highest sensitivity among all of the  
 1059 modes studied in previous searches [55]. Heavier neutralinos have similar results  
 1060 but generate less missing energy which reduces the efficiency of triggering.

1061 All of the simulated events are then reconstructed using the same software  
 1062 used for collision data. The fully reconstructed events are then reweighted to  
 1063 match the distribution of initial state radiation in an alternative sample of events,  
 1064 generated with MG5\_aMC@NLO [69], which has a more accurate description of ra-  
 1065 diate effects than Pythia6. This reweighting provides a more accurate descrip-  
 1066 tion of the momentum of the gluino-gluino system and is important in modeling  
 1067 the efficiency of triggering and offline event selection.



1068

1069 EVENT SELECTION

---

1070 The [LLPs](#) targeted by this search differ in their interactions with the detector from  
 1071 [SM](#) particles primarily because of their large mass. When produced at the ener-  
 1072 gies available at the [LHC](#), that large mass results in a low  $\beta$  (typically  $0.2 < \beta <$   
 1073  $0.9$ ). Such slow-moving particles heavily ionize in detector material. Each layer  
 1074 of the pixel detector provides a measurement of that ionization, through [ToT](#), as  
 1075 discussed in Section 6.3.1. The ionization in the pixel detector, quantified in  
 1076 terms of  $dE/dx$ , provides the major focus for this search technique, along with  
 1077 the momentum measured in the entire inner detector. It is effective both for its  
 1078 discriminating power and its use in reconstructing a particle's mass, and it can  
 1079 be used for a wide range of masses and lifetimes as discussed in Section 10.1.2.  
 1080 However  $dE/dx$  needs to be augmented with a few additional selection require-  
 1081 ments to provide a mechanism for triggering and to further reduce backgrounds.

1082 Ionization itself is not currently accessible for triggering, so this search in-  
 1083 stead relies on  $E_T^{\text{miss}}$  to trigger signal events. Although triggering on  $E_T^{\text{miss}}$  can  
 1084 be inefficient,  $E_T^{\text{miss}}$  is often large for many production mechanisms of [LLPs](#), as  
 1085 discussed in Section 10.1.

1086 The use of ionization to reject [SM](#) backgrounds relies on well-measured, high-  
 1087 momentum tracks, so some basic requirements on quality and kinematics are  
 1088 placed on the tracks considered in this search. These quality requirements have  
 1089 been significantly enhanced in Run 2 by a newly introduced tracking variable  
 1090 that is very effective in removing highly-ionizing backgrounds caused by over-  
 1091 lapping tracks. A few additional requirements are placed on the tracks consid-  
 1092 ered for [LLP](#) candidates that increase background rejection by targeting specific  
 1093 types of [SM](#) particles. These techniques provide a significant analysis improve-  
 1094 ment over previous iterations of ionization-based searches on ATLAS by provid-  
 1095 ing additional background rejection with minimal loss in signal efficiency.

1096 The ionization measurement with the Pixel detector can be calibrated to pro-  
 1097 vide an estimator of  $\beta\gamma$ . That estimate, together with the momentum measure-  
 1098 ment provided by tracking, can be used to reconstruct a mass for each track  
 1099 which traverses the pixel detector. That mass variable will be peaked at the [LLP](#)  
 1100 mass for any signal, and provides an additional tool to search for an excess. In  
 1101 addition to an explicit requirement on ionization, this search constructs a mass-  
 1102 window for each targeted signal mass in order to evaluate any excess of events  
 1103 and to set limits.

1104 The strategy discussed here is optimized for lifetimes of  $O(1) - O(10)$  ns.  
 1105 Pixel ionization is especially useful in this regime as particles only need to prop-  
 1106 agate through the first seven layers of the inner detector, about 37 cm from the  
 1107 beam axis. The search is still competitive with other searches for [LLPs](#) at longer  
 1108 lifetimes, because the primary discriminating variables are still applicable even  
 1109 for particles that do not decay within the detector [56]. Although the majority of

1110 the requirements will be the same for all lifetimes, two signal regions are defined  
 1111 to optimize separately for intermediate and long lifetime particles.

## 1112 11.1 TRIGGER

1113 Triggering remains a significant difficulty in defining an event selection with  
 1114 high signal efficiency in a search for [LLPs](#). There are no triggers available in  
 1115 the current ATLAS system that can fire directly from a high momentum track  
 1116 with large ionization (Section 6.6). Although in some configurations a charged  
 1117 [LLP](#) can fire muon triggers, this requirement introduces significant model depen-  
 1118 dence on both the allowed lifetimes and the interactions in the calorimeter [48],  
 1119 as discussed in Section 10.1.1.

1120 For a search targeting particles which may decay prior to reaching the muon  
 1121 system, the most efficient available trigger is based on missing energy [48]. As  
 1122 discussed in Section 10.1, signal events can produce significant  $E_T^{\text{miss}}$  by a few  
 1123 mechanisms. At the trigger level however, the missing energy is only calculated  
 1124 using the calorimeters (Section 6.6) where the R-Hadrons deposit little energy.  
 1125 So, at short lifetimes,  $E_T^{\text{miss}}$  measured in the calorimeter is generated by an im-  
 1126 balance between the jets and undetected [LSPs](#) produced in R-Hadron decays. At  
 1127 longer lifetimes, without the decay products, missing energy is only produced in  
 1128 the calorimeters when the R-Hadrons recoil against an initial state radiation ([ISR](#))  
 1129 jet.

1130 These features are highlighted in Figure ??, which shows the  $E_T^{\text{miss}}$  distribu-  
 1131 tions for simulated short lifetime (3 ns) and a stable R-Hadron events. The figure  
 1132 includes both the offline  $E_T^{\text{miss}}$ , the missing energy calculated with all available  
 1133 information, and Calorimeter  $E_T^{\text{miss}}$ , the missing energy calculated using only  
 1134 infomration available at the calorimeter which approximates the missing energy  
 1135 available at the trigger. **Note: Figuring is waiting on mc samples. I will add**  
 1136 **the figure and commentary asap. We will see that there is more full met**  
 1137 **than calomet in the stable case, but this won't always trigger. You can see**  
 1138 **this from a different perspective in the trigger efficiency plots below.**

1139 So, either case to some extent relies on kinematic degrees of freedom to pro-  
 1140 duce missing energy, as the pair-produced [LLPs](#) tend to balance each other in  
 1141 the transverse plain. That balance results in a relatively low efficiency for long-  
 1142 lifetime particles, roughly 40%, and efficiencies between 65% and 95% for shorter  
 1143 lifetimes depending on both the mass and the lifetime. For long lifetimes in par-  
 1144 ticular, the presence of [ISR](#) is important in providing an imbalance in the trans-  
 1145 verse plane, and is an important aspect of modeling the selection efficiency for  
 1146 R-Hadron events.

1147 The missing energy trigger with the lowest threshold available is chosen for  
 1148 this selection in order to maximize the trigger efficiency. During 2015 data col-  
 1149 lection this was the HLT\_xe70 trigger, which used a 50 GeV threshold on miss-  
 1150 ing energy at LVL1 and a 70 GeV threshold on missing energy at the HLT. These  
 1151 formation of the trigger decision for missing energy was discussed in more detail  
 1152 in Section 6.6.

## 1153 11.2 KINEMATICS AND ISOLATION

1154 After the trigger requirement, each event is required to have a primary vertex  
 1155 reconstructed from at least two well-measured tracks in the inner detector, each  
 1156 with  $p_T > 400$  MeV. If more than one such vertex exists, the primary vertex  
 1157 is taken to be the one with the largest summed track momentum for all tracks  
 1158 associated to that vertex. The offline reconstructed  $E_T^{\text{miss}}$  is required to be above  
 1159 130 GeV to additionally reject SM backgrounds. The transverse missing energy  
 1160 is calculated using fully reconstructed and calibrated offline objects, as described  
 1161 in Section 7.5. In particular the  $E_T^{\text{miss}}$  definition in this selection uses jets recon-  
 1162 structed with the anti- $k_t$  algorithm with radius  $R = 0.4$  from clusters of energy  
 1163 in the calorimeter (Section 7.2) and with  $p_T > 20$  GeV, as well as reconstructed  
 1164 muons, electrons, and tracks not identified as another object type.

1165 The  $E_T^{\text{miss}}$  distributions are shown for data and a few simulated signals in Fig-  
 1166 ure 27, after the trigger requirement. The cut placed at 130 GeV is 95% effi-  
 1167 cient for metastable and 90% efficient for stable particles, after the trigger re-  
 1168 quirement, because of the missing energy generating mechanisms discussed pre-  
 1169 viously. The distribution of data in this figure and subsequent figures in this sec-  
 1170 tion can be interpreted as the distribution of backgrounds, as any signal contam-  
 1171 ination would be negligible if present at these early stages of the selection (prior  
 1172 to the final requirement on ionization). The background falls rapidly with miss-  
 1173 ing energy, motivating the direct requirement on  $E_T^{\text{miss}}$  for the signal region. Al-  
 1174 though a tighter requirement than the specified value of 130 GeV would seem to  
 1175 increase the search potential from these early distributions, other requirements  
 1176 are more optimal when taken as a whole. The specific values for each require-  
 1177 ment in signal region were optimized considering the increase in discovery reach  
 1178 for tightening the requirement on each discriminating variable. **NOTE: If space**  
 1179 **and time permit, I will add a whole section about signal region optimiza-**  
 1180 **tion..**

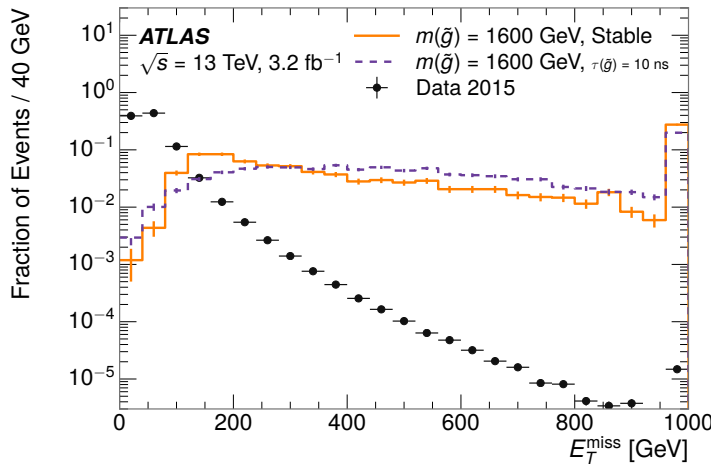


Figure 27: The distribution of  $E_T^{\text{miss}}$  for data and simulated signal events, after the trig-  
 ger requirement.

It is typically the practice for searches for new physics on ATLAS to place an offline requirement on the triggering variable that is sufficiently tight to guarantee that the event would pass the trigger. Such a tight requirement makes the uncertainty on the trigger efficiency of the simulation negligible, as modeling the regime where the trigger is only partially efficient can be difficult. In this analysis, however, because of the atypical interactions of R-Hadrons with the tracker and the calorimeter, the offline requirement on  $E_T^{\text{miss}}$  is not sufficient to guarantee a 100% trigger efficiency even at large values, as can be seen in Figure 28. This figure shows the efficiency for passing the HLT\_xe70 trigger as a function of the requirement on  $E_T^{\text{miss}}$ , which plateaus to roughly 85% even at large values. This plateau does not reach 100% because events which have large offline missing energy from a neutral R-Hadron produced opposite of a charged R-Hadron can have low missing energy in the calorimeters. The Calorimeter  $E_T^{\text{miss}}$ , on the other hand, does not have this effect and reaches 100% efficiency at large values because it is the quantity that directly corresponds to the trigger threshold. The systematic uncertainty that comes from using the events before the plateau is small because of the relatively good agreement between data and simulated events, as measured in decays of W-bosons, which is also shown in Figure 28. That small disagreement is later quantified and used as a systematic uncertainty on the signal efficiency. For these reasons, the requirement on  $E_T^{\text{miss}}$  is determined by optimizing the background rejection even though it corresponds to a value of trigger efficiency significantly below 1.0.

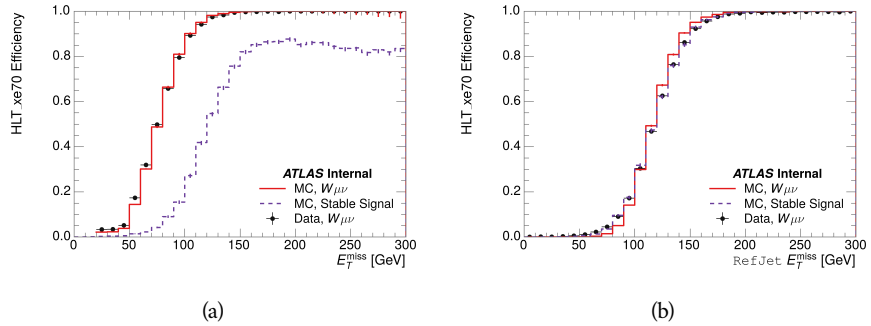


Figure 28: The trigger efficiency for the HLT\_xe70 trigger requirement as a function of (a)  $E_T^{\text{miss}}$  and (b) Calorimeter  $E_T^{\text{miss}}$  for simulated signal events. Data events with a W boson selection and simulated W boson events are also included.

Potential signal events are then required to have at least one candidate LLP track. Although the LLPs are produced in pairs, many models do not consistently yield two charged particles. For example, in the R-Hadron model highlighted here, only 20% of events have two charged R-Hadrons while 47% of events have just one. A signal region requiring two charged candidates could be a powerful improvement in background rejection for a larger dataset, but it is not considered in this version of the analysis as it was found to be unnecessary to reject the majority of backgrounds.

For a track to be selected as a candidate, it must have  $p_T > 50 \text{ GeV}$  and pass basic quality requirements. The track must be associated to the primary vertex.

1213 It must also have at least seven clusters in the silicon layers in the inner detector  
 1214 to ensure an accurate measurement of momentum. Those clusters must include  
 1215 one in the innermost layer if the extrapolated track is expected to pass through  
 1216 that layer. And to ensure a reliable measurement of ionization, the track is re-  
 1217 quired to have at least two clusters in the pixel detector that provide a measure-  
 1218 ment of  $dE/dx$ .

1219 At this point in the selection, there is a significant high-ionization background  
 1220 from multiple tracks that significantly overlap in the inner detector. Previous  
 1221 version of this analysis have rejected these overlaps by an explicit overlap rejec-  
 1222 tion between pairs of fully reconstructed tracks, typically by requiring no addi-  
 1223 tional tracks within a cone around the candidate. This technique, however, fails  
 1224 to remove the background from tracks that overlap so precisely that the tracks  
 1225 cannot be separately resolved, which can be produced in very collimated photon  
 1226 conversions or decays of pions.

1227 A new method, added in Run 2, identifies cluster shapes that are likely formed  
 1228 by multiple particles based on a neural network classification algorithm. The  
 1229 number of clusters that are classified this way in the pixel detector for a given  
 1230 track is called  $N_{\text{split}}$ . As the shape of clusters requires significantly less spatial  
 1231 separation to identify overlaps than it does to reconstruct two fully resolved  
 1232 tracks, this variable is more effective at rejecting backgrounds from overlaps.  
 1233 Figure 29 shows the dependence of ionization on  $N_{\text{split}}$ ; as  $N_{\text{split}}$  increases the  
 1234 most probable value of  $dE/dx$  grows significantly up to twice the expected value  
 1235 when  $N_{\text{split}} = 4$ .

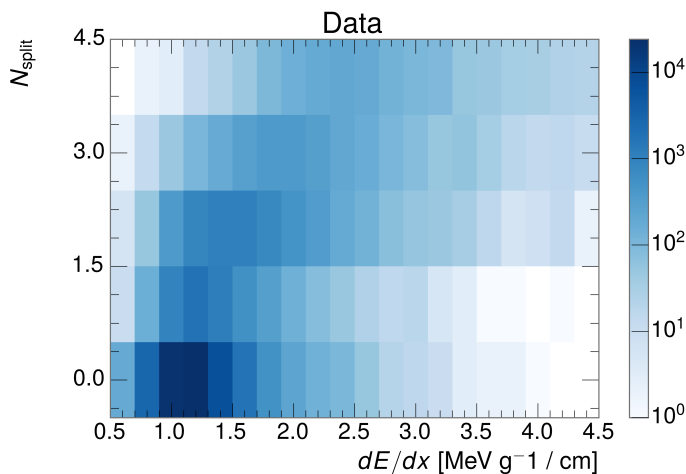


Figure 29: The dependence of  $dE/dx$  on  $N_{\text{split}}$  in data after basic track hit requirements  
 have been applied.

1236 This requirement is very successful in reducing the long positive tail of the  
 1237  $dE/dx$  distributions, as can be seen in Figure 30. Comparing the distribution  
 1238 for “baseline tracks”, tracks with only the above requirements on clusters ap-  
 1239 plied and before the requirement on  $N_{\text{split}}$ , to the distribution with  $N_{\text{split}} = 0$ ,  
 1240 it is clear that the fraction of tracks with large  $dE/dx$  is reduced be several or-  
 1241 ders of magnitude. The tracks without split hits are very close to the  $dE/dx$

1242 distribution of identified muons, which are extremely well isolated on average.  
 1243 Figure 30 also includes the distribution of  $dE/dx$  in an example signal simulation  
 1244 to demonstrate how effective  $dE/dx$  is as a discriminating variable with this  
 1245 isolation applied. The background falls rapidly for  $dE/dx > 1.8 \text{ MeV g}^{-1}\text{cm}^2$   
 1246 while the majority of the signal, approximately 90% depending on the mass, falls  
 1247 above that threshold. Over 90% of LLP tracks in simulated signal events pass the  
 1248  $N_{\text{split}}$ -based isolation requirement.

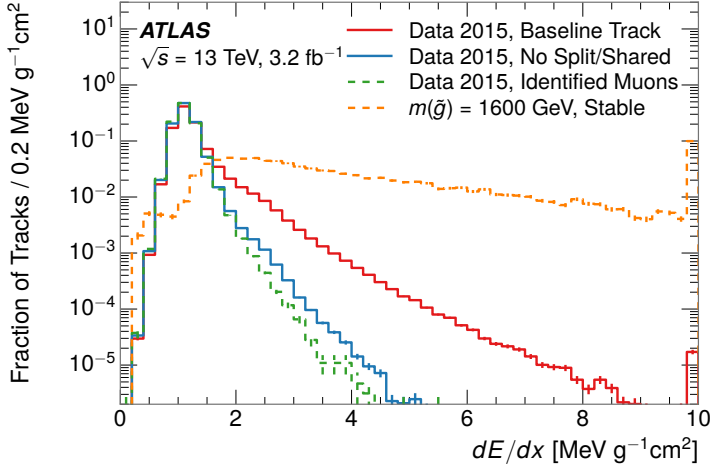


Figure 30: The distribution of  $dE/dx$  with various selections applied in data and simulated signal events.

1249 A few additional kinematic requirements are imposed to help reduce SM back-  
 1250 grounds. The momentum of the candidate track must be at least 150 GeV, and  
 1251 the uncertainty on that measurement must be less than 50%. The distribution of  
 1252 momentum is shown in Figure 31 for tracks in data and simulated signal events  
 1253 after the previously discussed requirements on clusters, transverse momentum,  
 1254 and isolation have been imposed. The signal particles are much harder on aver-  
 1255 age than their backgrounds because of the high energy interactions required to  
 1256 produce them. The transverse mass,  $M_T$ , defined as

$$M_T = \sqrt{2p_T E_T^{\text{miss}}(1 - \cos(\Delta\phi(E_T^{\text{miss}}, \text{track})))} \quad (1)$$

1257 estimates the mass of a decay of to a single charged particle and an undetected  
 1258 particle and is required to be greater than 130 GeV to reject contributions from  
 1259 the decay of W bosons. Figure 32 shows the distribution of  $M_T$  for data and  
 1260 simulated signal events. The signal is distributed over a wide range of  $M_T$ , with  
 1261 about 90% above the threshold value of 130 GeV. The data shows a dual-peaked  
 1262 structure, where the first peak comes from W boson decays and the second peak  
 1263 is a kinematic shaping from the requirements on  $E_T^{\text{miss}}$  and the track  $p_T$  in dijet  
 1264 events.

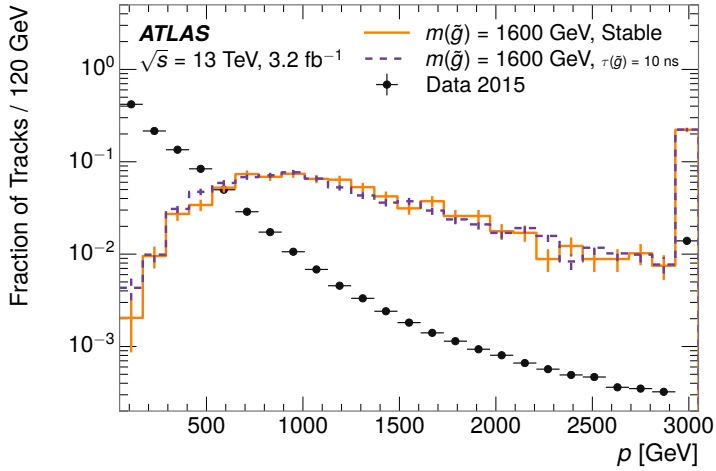


Figure 31: The distribution of track momentum for data and simulated signal events, after previous selection requirements have been applied.

## 1265 11.3 PARTICLE SPECIES REJECTION

1266 The amount of ionization deposited by particles with low mass and high momen-  
 1267 tum has a large positive tail [49], so backgrounds can be formed by a wide vari-  
 1268 ety of SM processes when various charged particles have a few randomly large  
 1269 deposits of energy in the pixel detector. Those backgrounds can be addition-  
 1270 ally reduced by targeting other interactions with the detector where they are  
 1271 expected to have different behavior than R-Hadrons. The interactions with the  
 1272 detector depend on the types of particles produced rather than the processes  
 1273 which produce them, so this search forms a series of rejections to remove back-  
 1274 grounds from individual particle species. These rejections focus on using addi-  
 1275 tional features of the event, other than the kinematics of the candidate track, as  
 1276 they can provide a powerful source of background rejection with very high sig-  
 1277 nal efficiency. However, the lifetime of an R-Hadron can significantly change its  
 1278 detector characteristics, as discussed in Section 10.1.2. To accommodate these  
 1279 differences, the SM rejections defined in this section are split to form two signal  
 1280 regions, one for long-lifetimes particles, the stable region ( $50 \leq \tau[\text{ns}] < \infty \text{ ns}$ ),  
 1281 and one for intermediate lifetime particles, the metastable region ( $0.4 < \tau[\text{ns}] <$   
 1282 50).

1283 Jets can be very effectively rejected by considering the larger-scale isolation of  
 1284 the candidate track. In this case the isolation focuses on the production of nearby  
 1285 particles as a jet-veto, rather than the isolation from overlapping tracks based on  
 1286  $N_{\text{split}}$  that was used to reduce high-ionization backgrounds. As explained in Sec-  
 1287 tion 10.1, the fragmentation process which produces an R-Hadron is very hard  
 1288 and thus is not expected to produce additional particles with a summed momen-  
 1289 tum of more than 5 GeV. The jet-veto uses the summed momentum of tracks  
 1290 with a cone of  $\Delta R < 0.25$ , referred to as  $p_T^{\text{Cone}}$ , which is shown in Figure 33 for  
 1291 data and simulated signal events. In the data this value has a peak at zero from  
 1292 isolated tracks such as leptons, and a long tail from jets which contains as much

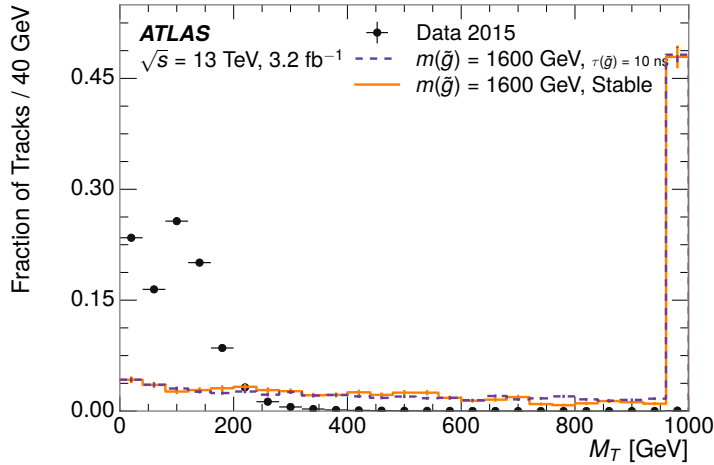


Figure 32: The distribution of  $M_T$  for data and simulated signal events, after previous selection requirements have been applied.

as 80% of the background above 20 GeV at this stage of the selection. In signal events  $p_T^{\text{Cone}}$  is strongly peaked at zero and significantly less than 1% of signal events have  $p_T^{\text{Cone}}$  above 20 GeV. This makes a requirement of  $p_T^{\text{Cone}} < 20 \text{ GeV}$  a very effective method to reject background without losing signal efficiency. For the stable signal region, this cut is further tightened to  $p_T^{\text{Cone}} < 5 \text{ GeV}$  as it is the most effective variable remaining to extend the search reach for long lifetimes.

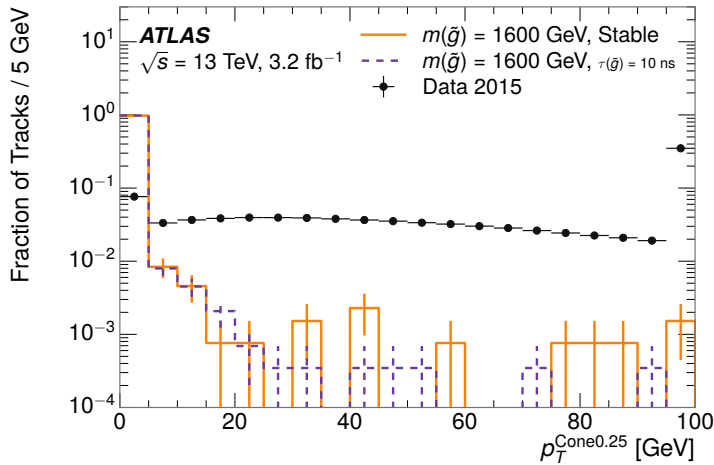


Figure 33: The distribution of summed tracked momentum within a cone of  $\Delta R < 0.25$  around the candidate track for data and simulated signal events, after previous selection requirements have been applied.

Even for fully isolated particles, there are additional methods to reject each type of particle using information in the muon system and calorimeters. Muons can be identified very reliably using the tracks in the muon system, as described in Section 7.4. For intermediate lifetimes the LLPs do not survive long enough

1304 to reach the muon system, and so muons are vetoed by rejecting tracks that as-  
 1305 sociate to a muon with medium muon identification requirements (Section 7.4).  
 1306 For longer lifetimes, this rejection is not applied because LLPs which reach the  
 1307 muon system can be identified as muons as often as 30% of the time in simulated  
 1308 samples.

1309 Calorimeter-based particle rejection relies on the expected small deposits of  
 1310 energy from LLPs. When the lifetime is long enough to reach the calorimeter, a  
 1311 LLP deposits little of its energy as it traverses the material, as discussed in Sec-  
 1312 tion 10.1. Even when the particle does decay before the calorimeter, the major-  
 1313 ity of its energy is carried away by the LSP and not deposited in the calorimeter.  
 1314 In both cases the energy is expected to be distributed across the layers of the  
 1315 calorimeters and not peaked in just one layer. This can be quantified in terms  
 1316 of  $E/p$ , the ratio of calorimeter energy of a nearby jet to the track momentum,  
 1317 and  $f_{EM}$ , the fraction of energy in that jet within the electromagnetic calorime-  
 1318 ter. When no jets fall within a cone of 0.05 of the particle,  $E/p$  and  $f_{EM}$  are both  
 1319 defined as zero.  $E/p$  is expected to be above 1.0 for typical SM particles because  
 1320 of calibration and the contributions from other nearby particles, as discussed in  
 1321 Chapter ???. At these momenta there is no significant zero fraction due to inter-  
 1322 actions with the detector or insufficient energy deposits (see Section 8.2.2).  $f_{EM}$   
 1323 is peaked close to 1.0 for electrons, and distributed between 10% and 90% for  
 1324 hadrons.

1325 These trends can be seen in the two dimensional distribution for signal in  
 1326 Figure 34 for stable and metastable (10 ns) events. The majority of R-Hadrons  
 1327 in both samples fall into the bin for  $E/p = 0$  and  $f_{EM} = 0$  because the majority  
 1328 of the time there is no associated jet. In the stable sample, when there often is  
 1329 an associated jet,  $E/p$  is typically still below 0.1, and the  $f_{EM}$  is predominantly  
 1330 under 0.8. In the metastable sample, on the other hand,  $E/p$  is larger but still  
 1331 typically below 0.1 because of actual jets produced during the decay. The  $f_{EM}$  is  
 1332 much lower on average in this case, below 0.1, because the 10 ns lifetime particles  
 1333 rarely decay before passing through the electromagnetic calorimeter. Figure 34  
 1334 also includes simulated Z decays to electrons or tau leptons. From the decays  
 1335 to electrons it is clear that the majority of electrons have  $f_{EM}$  above 0.9. The  
 1336 tau decays include a variety of products. Muons can be seen in the bin where  
 1337  $E/p = 0$  and  $f_{EM} = 0$  because they do not have an associated jet. Electrons fall  
 1338 into the range where  $E/p > 1$  and  $f_{EM} > 0.9$ . Hadronic tau decays are the most  
 1339 common, and fall in the range of  $0.1 < f_{EM} < 0.9$  and  $E/p > 1.0$ .

1340 These differences motivate an electron rejection by requiring an  $f_{EM}$  below  
 1341 0.9. Similarly, isolated hadrons are rejected by requiring  $E/p < 1.0$ . These re-  
 1342 quirements combine to remove the majority of isolated electrons and hadrons  
 1343 but retain over 95% of the simulated signal across a range of masses and lifetimes.

## 1344 11.4 IONIZATION

1345 The final requirement on the candidate track is the primary discriminating vari-  
 1346 able, the ionization in the pixel detector. That ionization is measured in terms  
 1347 of  $dE/dx$ , which was shown for data and simulated signal events in Figure 30.

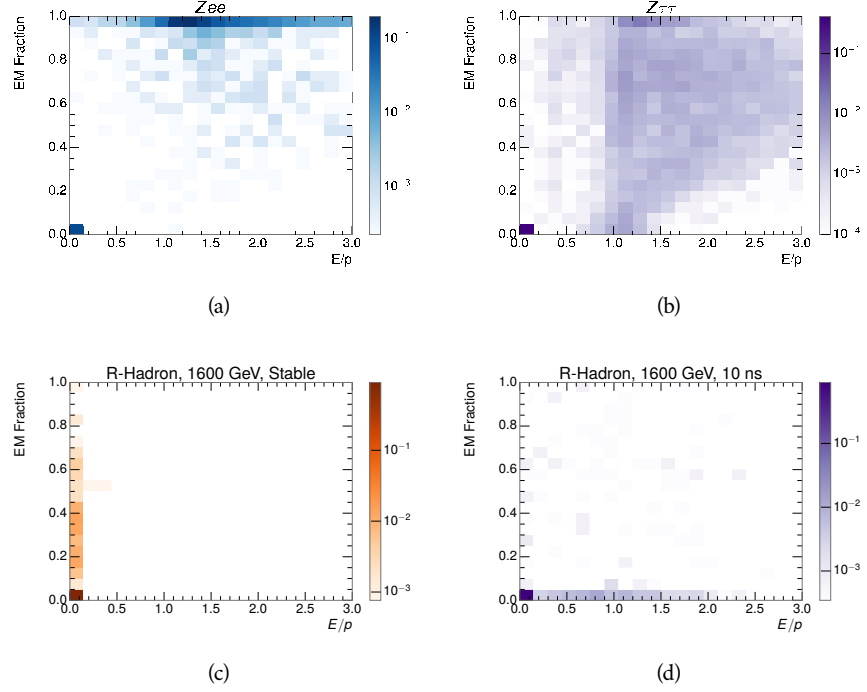


Figure 34: The normalized, two-dimensional distribution of  $E/p$  and  $f_{\text{EM}}$  for simulated (a)  $Z \rightarrow ee$ , (b)  $Z \rightarrow \tau\tau$ , (c) 1200 GeV Stable R-Hadron events, and (d) 1200 GeV, 10 ns R-Hadron events.

1348  $dE/dx$  is dramatically greater for the high mass signal particles than the back-  
 1349 grounds, which start to fall immediately after the minimally ionizing peak at 1.1  
 1350  $\text{MeV g}^{-1}\text{cm}^2$ . The  $dE/dx$  for candidate tracks must be greater than a pseudorapidity-  
 1351 dependent threshold, specifically  $1.80 - 0.11|\eta| + 0.17\eta^2 - 0.05\eta^3 \text{ MeV g}^{-1}\text{cm}^{-2}$ ,  
 1352 in order to correct for an approximately 5% dependence of the [MIP](#) peak on  $\eta$ .  
 1353 The requirement was chosen as part of the signal region optimization, and man-  
 1354 ages to reduce the backgrounds by a factor of 100 while remaining 70-90% effi-  
 1355 cient for simulated signal events depending on the mass.

1356 11.4.1 MASS ESTIMATION

1357 The mean value of ionization in silicon is governed by the Bethe equation and  
 1358 the most probable value follows a Landau-Vavilov distribution [49]. Those forms  
 1359 inspire a parametric description of  $dE/dx$  in terms of  $\beta\gamma$ ,

$$(dE/dx)_{\text{MPV}}(\beta\gamma) = \frac{p_1}{\beta^{p_3}} \ln(1 + [p_2\beta\gamma]^{p_5}) - p_4 \quad (2)$$

which performs well in the range  $0.3 < \beta\gamma < 1.5$ . This range includes the expected range of  $\beta\gamma$  for the particles targeted for this search, with  $\beta\gamma \approx 2.0$  for lower mass particles ( $O(100 \text{ GeV})$ ) and up to  $\beta\gamma \approx 0.5$  for higher mass particles ( $O(1000 \text{ GeV})$ ). The parameters,  $p_i$ , are fit using a 2015 data sample of low-momentum pions, kaons, and protons as described in Ref. [70]. Figure 35

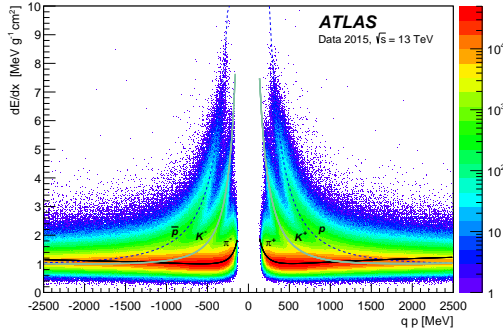


Figure 35: Two-dimensional distribution of  $dE/dx$  versus charge signed momentum ( $qp$ ) for minimum-bias tracks. The fitted distributions of the most probable values for pions, kaons and protons are superimposed.

1365 shows the two-dimensional distribution of  $dE/dx$  and momentum along with  
1366 the above fitted values for  $(dE/dx)_{MPV}$ .

1367 The above equation (2) is then numerically inverted to estimate  $\beta\gamma$  and the  
1368 mass for each candidate track. In simulated signal events, the mean of this mass  
1369 value reproduces the generated mass up to around 1800 GeV to within 3%, and  
1370 3% shift is applied to correct for this difference. The mass distributions prior to  
1371 this correction are shown for a few stable mass points in Figure 36. The large  
1372 widths of these distributions come from the high variability in energy deposits  
1373 in the pixel detector as well as the uncertainty on momentum measurements at  
1374 high momentum, but the means converge to the expected values.

1375 This analysis evaluates expected yields and the resulting cross sectional limits  
1376 using windows in this mass variable. The windows are formed by fitting mass  
1377 distributions in simulated signal events like those in Figure 36 to Gaussian distri-  
1378 butions and taking all events that fall within  $\pm 1.4\sigma$  of the mean. As can be seen  
1379 in Figure 36, typical values for this width are  $\sigma \approx 300 - 500$  GeV depending on  
1380 the generated mass.

## 1381 11.5 EFFICIENCY

1382 The numbers of events passing each requirement through ionization are shown  
1383 in Table 2 for the full 2015 dataset and a simulated 1600 GeV, 10 ns lifetime R-  
1384 Hadron sample. The table highlights the overall acceptance  $\times$  efficiency for sig-  
1385 nal events, which for this example is 19%. Between SM rejection and ionization,  
1386 this signal region reduces the background of tracks which pass the kinematic  
1387 requirements down by an additional factor of almost 2000.

1388 There is a strong dependence of this efficiency on lifetime and mass, with effi-  
1389 ciencies dropping to under 1% at low lifetimes. Figure 37 shows the dependence

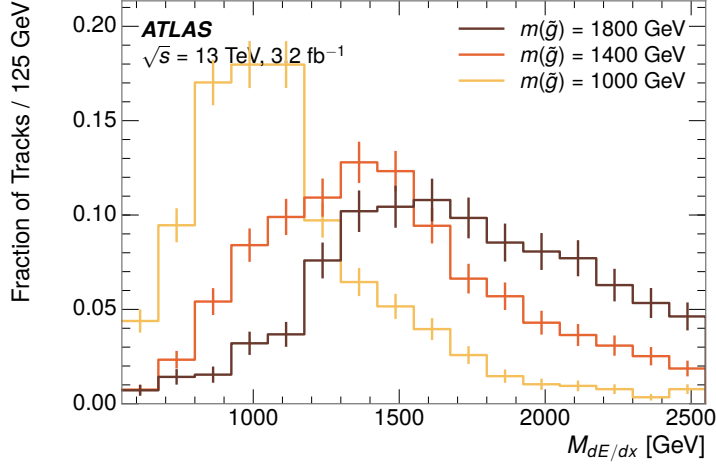


Figure 36: The distribution of mass estimated using  $dE/dx$  for simulated stable R-Hadrons with masses between 1000 and 1600 GeV.

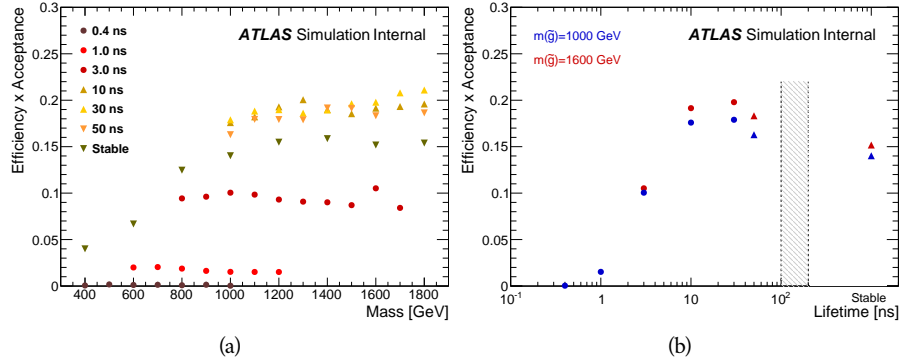


Figure 37: The acceptance  $\times$  efficiency as a function of R-Hadron (a) mass and (b) lifetime. (a) shows all of the combinations of mass and lifetime considered in this search, and (b) highlights the lifetime dependence for 1000 GeV and 1600 GeV R-Hadrons.

1390 on both mass and lifetime for all signal samples considered in this search. The  
 1391 dependence on mass is relatively slight and comes predominantly from the in-  
 1392 creasing fraction of R-Hadrons which pass the ionization cut with increasing  
 1393 mass. The trigger and  $E_T^{\text{miss}}$  requirements are most efficient for particles that  
 1394 decay before reaching the calorimeters. However, the chance of a particle to be  
 1395 reconstructed as a high-quality track decreases significantly at low lifetimes as  
 1396 the particle does not propagate sufficiently through the inner detector. These  
 1397 effects lead to a maximum in the selection efficiency for lifetimes around 10-30  
 1398 ns.

1399 The inefficiency of this signal region at short lifetimes comes almost exclu-  
 1400 sively from an acceptance effect, in that the particles do not reach the necessary  
 1401 layers of the SCT. This can be seen more clearly by defining a fiducial region  
 1402 which includes events with at least one R-Hadron that is produced with non-  
 1403 zero charge,  $p_T > 50 \text{ GeV}$ ,  $p > 150 \text{ GeV}$ ,  $|\eta| < 2.5$ , and a decay distance greater

Selection	Exp. Signal Events	Observed Events in $3.2 \text{ fb}^{-1}$
Generated	$26.0 \pm 0.3$	
$E_T^{\text{miss}}$ Trigger	$24.8 \pm 0.3$ (95%)	
$E_T^{\text{miss}} > 130 \text{ GeV}$	$23.9 \pm 0.3$ (92%)	
Track Quality and $p_T > 50$	$10.7 \pm 0.2$ (41%)	368324
Isolation Requirement	$9.0 \pm 0.2$ (35%)	108079
Track $p > 150 \text{ GeV}$	$6.6 \pm 0.2$ (25%)	47463
$M_T > 130 \text{ GeV}$	$5.8 \pm 0.2$ (22%)	18746
Electron and Hadron Veto	$5.5 \pm 0.2$ (21%)	3612
Muon Veto	$5.5 \pm 0.2$ (21%)	1668
Ionization Requirement	$5.0 \pm 0.1$ (19%)	11

Table 2: The expected number of events at each level of the selection for metastable  $1600 \text{ GeV}$ , 10 ns R-Hadrons, along with the number of events observed in data, for  $3.2 \text{ fb}^{-1}$ . The simulated yields are shown with statistical uncertainties only. The total efficiency  $\times$  acceptance is also shown for the signal.

<sup>1404</sup> than 37 cm in the transverse plane. At short (1 ns) lifetimes, the acceptance into  
<sup>1405</sup> this region is as low as 4%. Once this acceptance is accounted for, the selection  
<sup>1406</sup> efficiency ranges from 25% at lifetimes of 1 ns up to 45% at lifetimes of 10 ns.



1407

1408 BACKGROUND ESTIMATION

---

1409 The event selection discussed in the previous section focuses on detector signa-  
 1410 tures, emphasizing a single high-momentum, highly-ionizing track. That track  
 1411 is then required to be in some way inconsistent with the expected properties  
 1412 of SM particles, with various requirements designed to reject jets, hadrons,  
 1413 electrons, and muons (Section 11.3). Therefore the background for this search comes  
 1414 entirely from reducible backgrounds that are outliers of various distributions in-  
 1415 cluding  $dE/dx$ ,  $f_{EM}$ , and  $p_T^{\text{Cone}}$ . The simulation can be tuned in various ways to  
 1416 do an excellent job of modeling the average properties of each particle type [71],  
 1417 but it is not necessarily expected to accurately reproduce outliers. For this rea-  
 1418 sons, the background estimation used for this search is estimated entirely using  
 1419 data.

## 1420 12.1 BACKGROUND SOURCES

1421 SM charged particles with lifetimes long enough to form tracks in the inner de-  
 1422 tector can be grouped into three major categories based on their detector inter-  
 1423 actions: hadrons, electrons, and muons. Every particle that enters into the back-  
 1424 ground for this search belongs to one of these types. Relatively pure samples of  
 1425 tracks from each of these types can be formed in data by inverting the various  
 1426 rejection techniques in Section 11.3. Specifically, muons are selected requiring  
 1427 medium muon identification, electrons requiring  $E/p > 1.0$  and  $f_{EM} > 0.95$ ,  
 1428 and hadrons requiring  $E/p > 1.0$  and  $f_{EM} < 0.95$ .

1429 Figure 38 shows the distributions of momentum and  $dE/dx$  for these cate-  
 1430 gories in data, after requiring the event level selection as well as the track re-  
 1431 quirements on  $p_T$ , hits, and  $N_{\text{split}}$ , as discussed in Section 11.2. Simulated signal  
 1432 events are included for reference. These distribution are only illustrative of the  
 1433 differences between types, as the rejection requirements could alter their shape.  
 1434 This is especially significant for momentum which enters directly into  $E/p$  and  
 1435 can indirectly affect muon identification. However the various types show clear  
 1436 differences in both distributions. The distributions of momentum are not nec-  
 1437 essarily expected to match between the various types because the production  
 1438 mechanisms for each type result in different kinematic distributions.  $dE/dx$  is  
 1439 also different between types because of incomplete isolation; although the re-  
 1440 quirement on  $N_{\text{split}}$  helps to reduce the contribution of nearby particles it does  
 1441 not completely remove the effect of overlaps. Muons are better isolated because  
 1442 they do not have the additional particle from hadronization present for hadrons  
 1443 and they are significantly less likely to interact with the detector and produce  
 1444 secondary particles compared to hadrons and electrons. Thus muons have the  
 1445 smallest fraction of  $dE/dx$  above the threshold of  $1.8 \text{ MeVg}^{-1}\text{cm}^2$ ; hadrons and  
 1446 electrons have a larger fraction above this threshold.

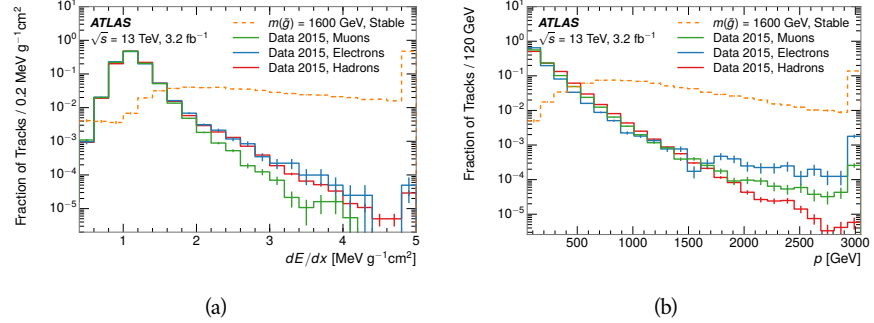


Figure 38: The distribution of (a)  $dE/dx$  and (b) momentum for tracks in data and simulated signal after requiring the event level selection and the track selection on  $p_T$ , hits, and  $N_{\text{split}}$ . Each sub-figure shows the normalized distributions for tracks classified as hadrons, electrons, and muons in data and R-Hadrons in the simulated signal.

1447 It is difficult to determine what fraction of each particle type enters into the fi-  
 1448 nal signal region. The background method will not have significant dependence  
 1449 on the relative contributions of each species, but it is useful to understand the  
 1450 differences between each when considering the various tests of the method.

## 1451 12.2 PREDICTION METHOD

1452 The data-driven background estimation relies on the independence between ion-  
 1453 ization and other kinematic variables in the event. For standard model particles  
 1454 with momenta above 50 GeV,  $dE/dx$  is not correlated with momentum; though  
 1455 there is a slight relativistic rise as momentum increases, the effect is small com-  
 1456 pared to the width of the distribution of ionization energy deposits.. So, the  
 1457 proposed method to estimate the mass distribution of the signal region is to use  
 1458 momentum from a track with low  $dE/dx$  (below the threshold value) and to com-  
 1459 bine it with a random  $dE/dx$  value from a  $dE/dx$  template. The resulting track is  
 1460 just as likely as the original, so a number of such random generations provide the  
 1461 expected distributions of momentum and ionization. These are then combined  
 1462 using the parametrization described in Section 11.4.1 to form a distribution of  
 1463 mass for the signal region.

1464 Algorithmically this method is implemented by forming two distinct Control  
 1465 Regions (**CR**s). The first **CR**, CR1, is formed by applying the entire event selec-  
 1466 tion from Chapter 11 up to the  $dE/dx$  and mass requirements. The  $dE/dx$  re-  
 1467 quirement is instead inverted for this region. Because of the independence of  
 1468  $dE/dx$ , the tracks in this control region have the same kinematic distribution  
 1469 as the tracks in the signal region, and are used to measure a two-dimensional  
 1470 template of  $p$  and  $\eta$ . The second **CR**, CR2, is formed from the event selection  
 1471 through the  $dE/dx$  requirement, but with an inverted  $E_T^{\text{miss}}$  requirement. The  
 1472 tracks in this control region are expected to have similar  $dE/dx$  distributions to  
 1473 the signal region before the ionization requirement, and so this region is used to  
 1474 measure a two-dimensional template of  $dE/dx$  and  $\eta$ .

1475 The contribution of any signal to the control regions is minimized by the in-  
 1476 verted selection requirements. Only less than 10% of simulated signal events  
 1477 have either  $dE/dx$  or  $E_T^{\text{miss}}$  below the threshold values in the original signal re-  
 1478 gion, while the backgrounds are significantly enhanced by inverting those re-  
 1479 quirements. The signal contamination is less than 1% in both control regions  
 1480 for all of the simulated masses and lifetimes considered in this analysis.

1481 With those measured templates, the shape of the mass estimation is generated  
 1482 by first selecting a random ( $p$ ,  $\eta$ ) combination from CR1. This momentum  
 1483 value is combined with a  $dE/dx$  value taken from the appropriate distribution  
 1484 of  $dE/dx$  for the selected  $\eta$  from CR2. The use of  $\eta$  in both random samplings  
 1485 controls for any correlation between  $p$ ,  $dE/dx$ , and  $\eta$ . Those values are then  
 1486 used to calculate a mass in the same way that is done for regular tracks in data,  
 1487 see Section 11.4.1. As this procedure includes all  $dE/dx$  values, the cut at 1.8  
 1488  $\text{MeVg}^{-1}\text{cm}^2$  is then enforced to fully model the signal region. The generated  
 1489 mass distribution is then normalized by scaling the background estimate to the  
 1490 data in the region  $M < 160 \text{ GeV}$ , where signals of this type have already been  
 1491 excluded [55]. This normalization uses the distributions of mass generated with-  
 1492 out the ionization requirement.

## 1493 12.3 VALIDATION

1494 The validity of the background estimation technique can be evaluated in both  
 1495 data and simulation. The underlying assumption that random combinations of  
 1496  $dE/dx$  and momentum can predict a mass distribution in an orthogonal region  
 1497 can be tested using simulated samples where concerns like multiple particle types  
 1498 can be controlled. Using the same technique in another set of signal-depleted  
 1499 regions in data then extends this confidence to the more complicated case where  
 1500 several particle species are inherently included.

### 1501 12.3.1 CLOSURE IN SIMULATION

1502 The first test of the procedure is done using a simulated sample of  $W \rightarrow \mu\nu$   
 1503 decays. These types of events provide the ingredients required to test the back-  
 1504 ground estimate,  $E_T^{\text{miss}}$  and isolated tracks, with high statistics. In this example  
 1505 there is no signal, so simulated events in the orthogonal CRs are used to estimate  
 1506 the shape of the mass distribution of the simulated events in the signal region. To  
 1507 reflect the different topology for W boson decays, the CRs use slightly modified  
 1508 definitions. In all CRs, the requirement of  $p > 150 \text{ GeV}$  and the SM rejection  
 1509 requirements are removed. Additionally, for the signal region the requirement  
 1510 on  $E_T^{\text{miss}}$  is relaxed to 30 GeV and the corresponding inverted requirement on  
 1511 CR2 is also set at 30 GeV.

1512 With these modified selections, the simulated and randomly generated distri-  
 1513 butions of  $M_{dE/dx}$  are shown in Figure 39. This figure includes the mass distri-  
 1514 butions before and after the requirement on  $dE/dx$ , which significantly shapes  
 1515 the distributions. In both cases the background estimation technique reproduces  
 1516 the shape of  $M_{dE/dx}$  in the signal region. There is a small difference in the pos-

itive tail of the mass distribution prior to the ionization cut, where the random events underestimate the fraction of tracks with mass above 150 GeV by about 20%. After the ionization requirement, however, this discrepancy is not present and the two distributions agree to within statistical uncertainties.

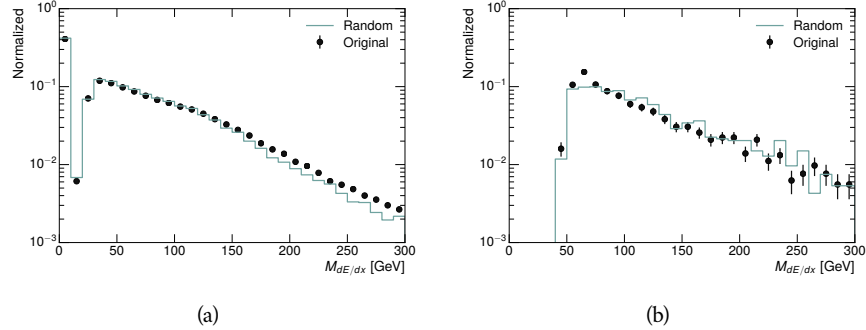


Figure 39: The distribution of  $M_{dE/dx}$  (a) before and (b) after the ionization requirement for tracks in simulated W boson decays and for the randomly generated background estimate.

This ability to reproduce the shape of the mass distribution in simulated events shows that the technique works as expected. No significant biases are acquired in using low  $dE/dx$  events to select kinematic templates or in using low  $E_T^{\text{miss}}$  events to select ionization templates, as either would result in a mismodeling of the shape of the mass distribution. The simulated events contain only one particle type, however, so this test only establishes that the technique works well when the the CRs are populated by exactly the same species.

### 1528 12.3.2 VALIDATION REGION IN DATA

The second test of the background estimate is performed using data in an orthogonal validation region. The validation region, and the corresponding CRs, are formed using the same selection requirements as in the nominal method but with a modified requirement on momentum,  $50 < p[\text{GeV}] < 150$ . This allows the technique to be checked in a region with very similar properties but where the signal is depleted, as the majority of the signal has momentum above 150 GeV while the backgrounds are enhanced below that threshold. Any biases on the particle composition of the CRs for the signal region will be reflected in the CRs used to estimate the mass distribution in the validation region.

Figure 40 shows the measured and randomly generated mass distributions for data before and after the ionization requirement. The background estimate does an excellent job of modeling the actual background before the ionization requirement, with good agreement to within the statistical uncertainties out to the limit of the mass distribution. There are very few events in the validation region after the ionization requirement, but the few observed events are consistent with the background prediction. The good agreement in this validation region provides a confirmation that the technique works even in the full-complexity case with

1546 multiple particle types entering the distributions. Any bias from changes in par-  
 1547 ticle composition between regions is small compared to statistical uncertainties.

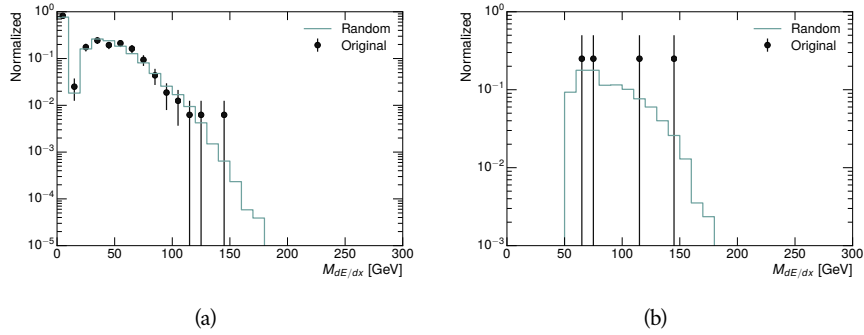


Figure 40: The distribution of  $M_{dE/dx}$  (a) before and (b) after the ionization requirement for tracks in the validation region and for the randomly generated background estimate.

[ September 19, 2016 at 11:30 – Version 0.35 ]

# 13

1548

1549 SYSTEMATIC UNCERTAINTIES AND RESULTS

---

1550 13.1 SYSTEMATIC UNCERTAINTIES

1551 13.2 FINAL YIELDS



# 14

1552

## 1553 INTERPRETATION

---

1554 14.1 CROSS SECTIONAL LIMITS

1555 14.2 MASS LIMITS

1556 14.3 CONTEXT FOR LONG-LIVED SEARCHES



1557

## PART VI

1558

### CONCLUSIONS

1559

You can put some informational part preamble text here.



# 15

1560

1561 SUMMARY AND OUTLOOK

---

1562 15.1 SUMMARY

1563 15.2 OUTLOOK



1564

## PART VII

1565

## APPENDIX

1566



# A

1567

1568 INELASTIC CROSS SECTION

---



# B

1569

## 1570 APPENDIX TEST

---

1571 Examples: *Italics*, SMALL CAPS, ALL CAPS <sup>1</sup>. Acronym testing: **UML!** (**UML!**) –  
1572 **UML! – UML! (UML!) – UML!s**

This appendix is temporary and is here to be used to check the style of the document.

### 1573 B.1 APPENDIX SECTION TEST

1574 Random text that should take up a few lines. The purpose is to see how sections  
1575 and subsections flow with some actual context. Without some body copy be-  
1576 tween each heading it can be difficult to tell if the weight of the fonts, styles, and  
1577 sizes use work well together.

#### 1578 B.1.1 APPENDIX SUBECTION TEST

1579 Random text that should take up a few lines. The purpose is to see how sections  
1580 and subsections flow with some actual context. Without some body copy be-  
1581 tween each heading it can be difficult to tell if the weight of the fonts, styles, and  
1582 sizes use work well together.

### 1583 B.2 A TABLE AND LISTING

1584 Curabitur tellus magna, porttitor a, commodo a, commodo in, tortor. Donec in-  
1585 terdum. Praesent scelerisque. Maecenas posuere sodales odio. Vivamus metus  
1586 lacus, varius quis, imperdiet quis, rhoncus a, turpis. Etiam ligula arcu, elemen-  
1587 tum a, venenatis quis, sollicitudin sed, metus. Donec nunc pede, tincidunt in,  
1588 venenatis vitae, faucibus vel, nibh. Pellentesque wisi. Nullam malesuada. Morbi  
1589 ut tellus ut pede tincidunt porta. Lorem ipsum dolor sit amet, consectetur adip-  
1590 iscing elit. Etiam congue neque id dolor.

1591 There is also a Python listing below Listing 1.

---

1 Footnote example.

LABITUR BONORUM PRI NO	QUE VISTA	HUMAN
fastidii ea ius	germano	demonstratea
suscipit instructior	titulo	personas
quaestio philosophia	facto	demonstrated

Table 3: Autem usu id.

## 1592 B.3 SOME FORMULAS

Due to the statistical nature of ionisation energy loss, large fluctuations can occur in the amount of energy deposited by a particle traversing an absorber element<sup>2</sup>. Continuous processes such as multiple scattering and energy loss play a relevant role in the longitudinal and lateral development of electromagnetic and hadronic showers, and in the case of sampling calorimeters the measured resolution can be significantly affected by such fluctuations in their active layers. The description of ionisation fluctuations is characterised by the significance parameter  $\kappa$ , which is proportional to the ratio of mean energy loss to the maximum allowed energy transfer in a single collision with an atomic electron:

*You might get unexpected results using math in chapter or section heads. Consider the pdfspacing option.*

$$\kappa = \frac{\xi}{E_{\max}} \quad (3)$$

$E_{\max}$  is the maximum transferable energy in a single collision with an atomic electron.

$$E_{\max} = \frac{2m_e\beta^2\gamma^2}{1 + 2\gamma m_e/m_x + (m_e/m_x)^2},$$

1593 where  $\gamma = E/m_x$ ,  $E$  is energy and  $m_x$  the mass of the incident particle,  $\beta^2 = 1 - 1/\gamma^2$  and  $m_e$  is the electron mass.  $\xi$  comes from the Rutherford scattering cross section and is defined as:

$$\xi = \frac{2\pi z^2 e^4 N_{Av} Z \rho \delta x}{m_e \beta^2 c^2 A} = 153.4 \frac{z^2}{\beta^2} \frac{Z}{A} \rho \delta x \text{ keV},$$

1596 where

- z charge of the incident particle
- $N_{Av}$  Avogadro's number
- Z atomic number of the material
- A atomic weight of the material
- $\rho$  density
- $\delta x$  thickness of the material
- 1598  $\kappa$  measures the contribution of the collisions with energy transfer close to  
1599  $E_{\max}$ . For a given absorber,  $\kappa$  tends towards large values if  $\delta x$  is large and/or if  
1600  $\beta$  is small. Likewise,  $\kappa$  tends towards zero if  $\delta x$  is small and/or if  $\beta$  approaches  
1601 1.

2 Examples taken from Walter Schmidt's great gallery:  
<http://home.vrweb.de/~was/mathfonts.html>

Listing 1: A floating example (listings manual)

---

```
1 for i in xrange(10):
    print i, i*i, i*i*i
print "done"
```

---

1602      The value of  $\kappa$  distinguishes two regimes which occur in the description of  
1603      ionisation fluctuations:

- 1604      1. A large number of collisions involving the loss of all or most of the incident  
1605      particle energy during the traversal of an absorber.

1606      As the total energy transfer is composed of a multitude of small energy  
1607      losses, we can apply the central limit theorem and describe the fluctua-  
1608      tions by a Gaussian distribution. This case is applicable to non-relativistic  
1609      particles and is described by the inequality  $\kappa > 10$  (i. e., when the mean en-  
1610      ergy loss in the absorber is greater than the maximum energy transfer in  
1611      a single collision).

- 1612      2. Particles traversing thin counters and incident electrons under any condi-  
1613      tions.

1614      The relevant inequalities and distributions are  $0.01 < \kappa < 10$ , Vavilov  
1615      distribution, and  $\kappa < 0.01$ , Landau distribution.



- 1617 [1] S. Agostinelli et al. “GEANT4: A simulation toolkit”. In: *Nucl. Instrum. Meth.*  
1618 A 506 (2003), pp. 250–303. doi: [10.1016/S0168-9002\(03\)01368-8](https://doi.org/10.1016/S0168-9002(03)01368-8).
- 1619 [2] ATLAS Collaboration. “A study of the material in the ATLAS inner de-  
1620 tector using secondary hadronic interactions”. In: *JINST* 7 (2012), P01013.  
1621 doi: [10.1088/1748-0221/7/01/P01013](https://doi.org/10.1088/1748-0221/7/01/P01013). arXiv: [1110.6191 \[hep-ex\]](https://arxiv.org/abs/1110.6191).  
1622 PERF-2011-08.
- 1623 [3] ATLAS Collaboration. “Electron and photon energy calibration with the  
1624 ATLAS detector using LHC Run 1 data”. In: *Eur. Phys. J. C* 74 (2014), p. 3071.  
1625 doi: [10.1140/epjc/s10052-014-3071-4](https://doi.org/10.1140/epjc/s10052-014-3071-4). arXiv: [1407.5063](https://arxiv.org/abs/1407.5063)  
1626 [hep-ex]. PERF-2013-05.
- 1627 [4] ATLAS Collaboration. “A measurement of the calorimeter response to sin-  
1628 ggle hadrons and determination of the jet energy scale uncertainty using  
1629 LHC Run-1  $pp$ -collision data with the ATLAS detector”. In: (2016). arXiv:  
1630 [1607.08842 \[hep-ex\]](https://arxiv.org/abs/1607.08842). PERF-2015-05.
- 1631 [5] ATLAS Collaboration. “Single hadron response measurement and calorime-  
1632 ter jet energy scale uncertainty with the ATLAS detector at the LHC”. In:  
1633 *Eur. Phys. J. C* 73 (2013), p. 2305. doi: [10.1140/epjc/s10052-013-2305-1](https://doi.org/10.1140/epjc/s10052-013-2305-1). arXiv: [1203.1302 \[hep-ex\]](https://arxiv.org/abs/1203.1302). PERF-2011-05.
- 1635 [6] ATLAS Collaboration. “The ATLAS Simulation Infrastructure”. In: *Eur.*  
1636 *Phys. J. C* 70 (2010), p. 823. doi: [10.1140/epjc/s10052-010-1429-9](https://doi.org/10.1140/epjc/s10052-010-1429-9).  
1637 arXiv: [1005.4568 \[hep-ex\]](https://arxiv.org/abs/1005.4568). SOFT-2010-01.
- 1638 [7] T. Sjöstrand, S. Mrenna, and P. Skands. “A Brief Introduction to PYTHIA  
1639 8.1”. In: *Comput. Phys. Commun.* 178 (2008), pp. 852–867. doi: [10.1016/j.cpc.2008.01.036](https://doi.org/10.1016/j.cpc.2008.01.036). arXiv: [0710.3820](https://arxiv.org/abs/0710.3820).
- 1641 [8] ATLAS Collaboration. *Summary of ATLAS Pythia 8 tunes*. ATL-PHYS-PUB-  
1642 2012-003. 2012. URL: <http://cds.cern.ch/record/1474107>.
- 1643 [9] A.D. Martin, W.J. Stirling, R.S. Thorne, and G. Watt. “Parton distributions  
1644 for the LHC”. In: *Eur. Phys. J. C* 63 (2009). Figures from the [MSTW Website](#),  
1645 pp. 189–285. doi: [10.1140/epjc/s10052-009-1072-5](https://doi.org/10.1140/epjc/s10052-009-1072-5). arXiv: [0901.0002](https://arxiv.org/abs/0901.0002).
- 1647 [10] A. Sherstnev and R.S. Thorne. “Parton Distributions for LO Generators”.  
1648 In: *Eur. Phys. J. C* 55 (2008), pp. 553–575. doi: [10.1140/epjc/s10052-008-0610-x](https://doi.org/10.1140/epjc/s10052-008-0610-x). arXiv: [0711.2473](https://arxiv.org/abs/0711.2473).
- 1650 [11] A. Ribon et al. *Status of Geant4 hadronic physics for the simulation of LHC*  
1651 *experiments at the start of LHC physics program*. CERN-LCGAPP-2010-02.  
1652 2010. URL: <http://lcgapp.cern.ch/project/docs/noteStatusHadronic2010.pdf>.

- 1654 [12] M. P. Guthrie, R. G. Alsmiller, and H. W. Bertini. "Calculation of the cap-  
 1655 ture of negative pions in light elements and comparison with experiments  
 1656 pertaining to cancer radiotherapy". In: *Nucl. Instrum. Meth.* 66 (1968), pp. 29–  
 1657 36. doi: [10.1016/0029-554X\(68\)90054-2](https://doi.org/10.1016/0029-554X(68)90054-2).
- 1658 [13] H. W. Bertini and P. Guthrie. "News item results from medium-energy  
 1659 intranuclear-cascade calculation". In: *Nucl. Instr. and Meth. A* 169 (1971),  
 1660 p. 670. doi: [10.1016/0375-9474\(71\)90710-X](https://doi.org/10.1016/0375-9474(71)90710-X).
- 1661 [14] V.A. Karmanov. "Light Front Wave Function of Relativistic Composite  
 1662 System in Explicitly Solvable Model". In: *Nucl. Phys. B* 166 (1980), p. 378.  
 1663 doi: [10.1016/0550-3213\(80\)90204-7](https://doi.org/10.1016/0550-3213(80)90204-7).
- 1664 [15] H. S. Fesefeldt. *GHEISHA program*. Pitha-85-02, Aachen. 1985.
- 1665 [16] G. Folger and J.P. Wellisch. "String parton models in Geant4". In: (2003).  
 1666 arXiv: [nucl-th/0306007](https://arxiv.org/abs/nucl-th/0306007).
- 1667 [17] N. S. Amelin et al. "Transverse flow and collectivity in ultrarelativistic  
 1668 heavy-ion collisions". In: *Phys. Rev. Lett.* 67 (1991), p. 1523. doi: [10.1103/PhysRevLett.67.1523](https://doi.org/10.1103/PhysRevLett.67.1523).
- 1670 [18] N. S. Amelin et al. "Collectivity in ultrarelativistic heavy ion collisions". In:  
 1671 *Nucl. Phys. A* 544 (1992), p. 463. doi: [10.1016/0375-9474\(92\)90598-E](https://doi.org/10.1016/0375-9474(92)90598-E).
- 1673 [19] L. V. Bravina et al. "Fluid dynamics and Quark Gluon string model - What  
 1674 we can expect for Au+Au collisions at 11.6 AGeV/c". In: *Nucl. Phys. A* 566  
 1675 (1994), p. 461. doi: [10.1016/0375-9474\(94\)90669-6](https://doi.org/10.1016/0375-9474(94)90669-6).
- 1676 [20] L. V. Bravin et al. "Scaling violation of transverse flow in heavy ion colli-  
 1677 sions at AGS energies". In: *Phys. Lett. B* 344 (1995), p. 49. doi: [10.1016/0370-2693\(94\)01560-Y](https://doi.org/10.1016/0370-2693(94)01560-Y).
- 1679 [21] B. Andersson et al. "A model for low-pT hadronic reactions with general-  
 1680 izations to hadron-nucleus and nucleus-nucleus collisions". In: *Nucl. Phys.*  
 1681 *B* 281 (1987), p. 289. doi: [10.1016/0550-3213\(87\)90257-4](https://doi.org/10.1016/0550-3213(87)90257-4).
- 1682 [22] B. Andersson, A. Tai, and B.-H. Sa. "Final state interactions in the (nuclear)  
 1683 FRITIOF string interaction scenario". In: *Z. Phys. C* 70 (1996), pp. 499–  
 1684 506. doi: [10.1007/s002880050127](https://doi.org/10.1007/s002880050127).
- 1685 [23] B. Nilsson-Almqvist and E. Stenlund. "Interactions Between Hadrons and  
 1686 Nuclei: The Lund Monte Carlo, Fritiof Version 1.6". In: *Comput. Phys. Com-*  
 1687 *mun.* 43 (1987), p. 387. doi: [10.1016/0010-4655\(87\)90056-7](https://doi.org/10.1016/0010-4655(87)90056-7).
- 1688 [24] B. Ganhuyag and V. Uzhinsky. "Modified FRITIOF code: Negative charged  
 1689 particle production in high energy nucleus nucleus interactions". In: *Czech.*  
 1690 *J. Phys.* 47 (1997), pp. 913–918. doi: [10.1023/A:1021296114786](https://doi.org/10.1023/A:1021296114786).
- 1691 [25] ATLAS Collaboration. "Topological cell clustering in the ATLAS calorime-  
 1692 ters and its performance in LHC Run 1". In: (2016). arXiv: [1603.02934](https://arxiv.org/abs/1603.02934)  
 1693 [[hep-ex](#)].
- 1694 [26] Peter Speckmayer. "Energy Measurement of Hadrons with the CERN AT-  
 1695 LAS Calorimeter". Presented on 18 Jun 2008. PhD thesis. Vienna: Vienna,  
 1696 Tech. U., 2008. URL: <http://cds.cern.ch/record/1112036>.

- 1697 [27] CMS Collaboration. “The CMS barrel calorimeter response to particle  
1698 beams from 2 to 350 GeV/c”. In: *Eur. Phys. J. C* 60.3 (2009). doi: [10.1140/epjc/s10052-009-0959-5](https://doi.org/10.1140/epjc/s10052-009-0959-5).
- 1700 [28] J. Beringer et al. (Particle Data Group). “Review of Particle Physics”. In:  
1701 *Chin. Phys. C* 38 (2014), p. 090001. URL: <http://pdg.lbl.gov>.
- 1702 [29] P. Adragna et al. “Measurement of Pion and Proton Response and Lon-  
1703 gitudinal Shower Profiles up to 20 Nuclear Interaction Lengths with the  
1704 ATLAS Tile Calorimeter”. In: *Nucl. Instrum. Meth. A* 615 (2010), pp. 158–  
1705 181. doi: [10.1016/j.nima.2010.01.037](https://doi.org/10.1016/j.nima.2010.01.037).
- 1706 [30] ATLAS Collaboration. “Jet energy measurement and its systematic uncer-  
1707 tainty in proton–proton collisions at  $\sqrt{s} = 7$  TeV with the ATLAS detec-  
1708 tor”. In: *Eur. Phys. J. C* 75 (2015), p. 17. doi: [10.1140/epjc/s10052-014-3190-y](https://doi.org/10.1140/epjc/s10052-014-3190-y). arXiv: [1406.0076 \[hep-ex\]](https://arxiv.org/abs/1406.0076). PERF-2012-01.
- 1710 [31] Hung-Liang Lai, Marco Guzzi, Joey Huston, Zhao Li, Pavel M. Nadolsky,  
1711 et al. “New parton distributions for collider physics”. In: *Phys. Rev. D* 82  
1712 (2010), p. 074024. doi: [10.1103/PhysRevD.82.074024](https://doi.org/10.1103/PhysRevD.82.074024). arXiv: [1007.2241 \[hep-ph\]](https://arxiv.org/abs/1007.2241).
- 1714 [32] E. Abat et al. “Study of energy response and resolution of the ATLAS barrel  
1715 calorimeter to hadrons of energies from 20 to 350 GeV”. In: *Nucl. Instrum.*  
1716 *Meth. A* 621.1-3 (2010), pp. 134 – 150. doi: <http://dx.doi.org/10.1016/j.nima.2010.04.054>.
- 1718 [33] ATLAS Collaboration. “Jet energy measurement with the ATLAS detector  
1719 in proton–proton collisions at  $\sqrt{s} = 7$  TeV”. In: *Eur. Phys. J. C* 73 (2013),  
1720 p. 2304. doi: [10.1140/epjc/s10052-013-2304-2](https://doi.org/10.1140/epjc/s10052-013-2304-2). arXiv: [1112.6426 \[hep-ex\]](https://arxiv.org/abs/1112.6426). PERF-2011-03.
- 1722 [34] Nausheen R. Shah and Carlos E. M. Wagner. “Gravitons and dark matter in  
1723 universal extra dimensions”. In: *Phys. Rev. D* 74 (2006), p. 104008. doi: [10.1103/PhysRevD.74.104008](https://doi.org/10.1103/PhysRevD.74.104008). arXiv: [hep-ph/0608140 \[hep-ph\]](https://arxiv.org/abs/hep-ph/0608140).
- 1725 [35] Jonathan L. Feng, Arvind Rajaraman, and Fumihiro Takayama. “Graviton  
1726 cosmology in universal extra dimensions”. In: *Phys. Rev. D* 68 (2003), p. 085018.  
1727 doi: [10.1103/PhysRevD.68.085018](https://doi.org/10.1103/PhysRevD.68.085018). arXiv: [hep-ph/0307375 \[hep-ph\]](https://arxiv.org/abs/hep-ph/0307375).
- 1729 [36] Paul H. Frampton and Pham Quang Hung. “Long-lived quarks?” In: *Phys.*  
1730 *Rev. D* 58 (5 1998), p. 057704. doi: [10.1103/PhysRevD.58.057704](https://doi.org/10.1103/PhysRevD.58.057704).  
1731 URL: <http://link.aps.org/doi/10.1103/PhysRevD.58.057704>.
- 1733 [37] C. Friberg, E. Norrbin, and T. Sjostrand. “QCD aspects of leptoquark pro-  
1734 duction at HERA”. In: *Phys. Lett. B* 403 (1997), pp. 329–334. doi: [10.1016/S0370-2693\(97\)00543-1](https://doi.org/10.1016/S0370-2693(97)00543-1). arXiv: [hep-ph/9704214 \[hep-ph\]](https://arxiv.org/abs/hep-ph/9704214).
- 1736 [38] Herbert K. Dreiner. “An introduction to explicit R-parity violation”. In:  
1737 (1997). arXiv: [hep-ph/9707435](https://arxiv.org/abs/hep-ph/9707435).

- 1738 [39] Edmond L. Berger and Zack Sullivan. “Lower limits on R-parity-violating  
 1739 couplings in supersymmetry”. In: *Phys. Rev. Lett.* 92 (2004), p. 201801. doi:  
 1740 [10.1103/PhysRevLett.92.201801](https://doi.org/10.1103/PhysRevLett.92.201801). arXiv: [hep-ph/0310001](https://arxiv.org/abs/hep-ph/0310001).
- 1741 [40] R. Barbieri, C. Berat, M. Besancon, M. Chemtob, A. Deandrea, et al. “R-  
 1742 parity violating supersymmetry”. In: *Phys. Rept.* 420 (2005), p. 1. doi: [10.1016/j.physrep.2005.08.006](https://doi.org/10.1016/j.physrep.2005.08.006). arXiv: [hep-ph/0406039](https://arxiv.org/abs/hep-ph/0406039).
- 1744 [41] M. Fairbairn et al. “Stable massive particles at colliders”. In: *Phys. Rept.* 438  
 1745 (2007), p. 1. doi: [10.1016/j.physrep.2006.10.002](https://doi.org/10.1016/j.physrep.2006.10.002). arXiv: [hep-ph/0611040](https://arxiv.org/abs/hep-ph/0611040).
- 1747 [42] Christopher F. Kolda. “Gauge-mediated supersymmetry breaking: Intro-  
 1748 duction, review and update”. In: *Nucl. Phys. Proc. Suppl.* 62 (1998), p. 266.  
 1749 doi: [10.1016/S0920-5632\(97\)00667-1](https://doi.org/10.1016/S0920-5632(97)00667-1). arXiv: [hep-ph/9707450](https://arxiv.org/abs/hep-ph/9707450).
- 1750 [43] Howard Baer, Kingman Cheung, and John F. Gunion. “A Heavy gluino as  
 1751 the lightest supersymmetric particle”. In: *Phys. Rev. D* 59 (1999), p. 075002.  
 1752 doi: [10.1103/PhysRevD.59.075002](https://doi.org/10.1103/PhysRevD.59.075002). arXiv: [hep-ph/9806361](https://arxiv.org/abs/hep-ph/9806361).
- 1753 [44] S. James Gates Jr. and Oleg Lebedev. “Searching for supersymmetry in  
 1754 hadrons”. In: *Phys. Lett. B* 477 (2000), p. 216. doi: [10.1016/S0370-2693\(00\)00172-6](https://doi.org/10.1016/S0370-2693(00)00172-6). arXiv: [hep-ph/9912362](https://arxiv.org/abs/hep-ph/9912362).
- 1756 [45] G. F. Giudice and A. Romanino. “Split supersymmetry”. In: *Nucl. Phys. B*  
 1757 699 (2004), p. 65. doi: [10.1016/j.nuclphysb.2004.11.048](https://doi.org/10.1016/j.nuclphysb.2004.11.048). arXiv:  
 1758 [hep-ph/0406088](https://arxiv.org/abs/hep-ph/0406088).
- 1759 [46] N. Arkani-Hamed, S. Dimopoulos, G. F. Giudice, and A. Romanino. “As-  
 1760 pects of split supersymmetry”. In: *Nucl. Phys. B* 709 (2005), p. 3. doi: [10.1016/j.nuclphysb.2004.12.026](https://doi.org/10.1016/j.nuclphysb.2004.12.026). arXiv: [hep-ph/0409232](https://arxiv.org/abs/hep-ph/0409232).
- 1762 [47] Glennys R. Farrar and Pierre Fayet. “Phenomenology of the Production,  
 1763 Decay, and Detection of New Hadronic States Associated with Supersym-  
 1764 metry”. In: *Phys. Lett.* B76 (1978), pp. 575–579. doi: [10.1016/0370-2693\(78\)90858-4](https://doi.org/10.1016/0370-2693(78)90858-4).
- 1766 [48] A. C. Kraan, J. B. Hansen, and P. Nevski. “Discovery potential of R-hadrons  
 1767 with the ATLAS detector”. In: *Eur. Phys. J.* C49 (2007), pp. 623–640. doi:  
 1768 [10.1140/epjc/s10052-006-0162-x](https://doi.org/10.1140/epjc/s10052-006-0162-x). arXiv: [hep-ex/0511014](https://arxiv.org/abs/hep-ex/0511014)  
 1769 [[hep-ex](#)].
- 1770 [49] K. A. Olive et al. “Review of Particle Physics”. In: *Chin. Phys.* C38 (2014),  
 1771 p. 090001. doi: [10.1088/1674-1137/38/9/090001](https://doi.org/10.1088/1674-1137/38/9/090001).
- 1772 [50] Rasmus Mackeprang and David Milstead. “An Updated Description of  
 1773 Heavy-Hadron Interactions in GEANT-4”. In: *Eur. Phys. J.* C66 (2010), pp. 493–  
 1774 501. doi: [10.1140/epjc/s10052-010-1262-1](https://doi.org/10.1140/epjc/s10052-010-1262-1). arXiv: [0908.1868](https://arxiv.org/abs/0908.1868)  
 1775 [[hep-ph](#)].
- 1776 [51] ATLAS Collaboration. “Search for massive, long-lived particles using mul-  
 1777 titrack displaced vertices or displaced lepton pairs in  $pp$  collisions at  $\sqrt{s} =$   
 1778 8 TeV with the ATLAS detector”. In: *Phys. Rev. D* 92 (2015), p. 072004.  
 1779 doi: [10.1103/PhysRevD.92.072004](https://doi.org/10.1103/PhysRevD.92.072004). arXiv: [1504.05162](https://arxiv.org/abs/1504.05162) [[hep-ex](#)].  
 1780 SUSY-2014-02.

- 1781 [52] ATLAS Collaboration. “Search for charginos nearly mass degenerate with  
 1782 the lightest neutralino based on a disappearing-track signature in  $pp$  col-  
 1783 lisions at  $\sqrt{s} = 8$  TeV with the ATLAS detector”. In: *Phys. Rev. D* 88 (2013),  
 1784 p. 112006. doi: [10.1103/PhysRevD.88.112006](https://doi.org/10.1103/PhysRevD.88.112006). arXiv: [1310.3675](https://arxiv.org/abs/1310.3675)  
 1785 [[hep-ex](#)]. SUSY-2013-01.
- 1786 [53] ATLAS Collaboration. “Searches for heavy long-lived sleptons and R-Hadrons  
 1787 with the ATLAS detector in  $pp$  collisions at  $\sqrt{s} = 7$  TeV”. In: *Phys. Lett. B*  
 1788 720 (2013), p. 277. doi: [10.1016/j.physletb.2013.02.015](https://doi.org/10.1016/j.physletb.2013.02.015). arXiv:  
 1789 [1211.1597](https://arxiv.org/abs/1211.1597) [[hep-ex](#)]. SUSY-2012-01.
- 1790 [54] ATLAS Collaboration. “Searches for heavy long-lived charged particles  
 1791 with the ATLAS detector in proton–proton collisions at  $\sqrt{s} = 8$  TeV”. In: *JHEP* 01 (2015), p. 068. doi: [10.1007/JHEP01\(2015\)068](https://doi.org/10.1007/JHEP01(2015)068). arXiv:  
 1792 [1411.6795](https://arxiv.org/abs/1411.6795) [[hep-ex](#)]. SUSY-2013-22.
- 1793 [55] ATLAS Collaboration. “Search for metastable heavy charged particles with  
 1794 large ionisation energy loss in  $pp$  collisions at  $\sqrt{s} = 8$  TeV using the AT-  
 1795 LAS experiment”. In: *Eur. Phys. J. C* 75 (2015), p. 407. doi: [10.1140/epjc/s10052-015-3609-0](https://doi.org/10.1140/epjc/s10052-015-3609-0). arXiv: [1506.05332](https://arxiv.org/abs/1506.05332) [[hep-ex](#)]. SUSY-  
 1796 2014-09.
- 1797 [56] ATLAS Collaboration. “Search for heavy long-lived charged  $R$ -hadrons  
 1798 with the ATLAS detector in  $3.2 \text{ fb}^{-1}$  of proton–proton collision data at  
 1799  $\sqrt{s} = 13$  TeV”. In: *Phys. Lett. B* 760 (2016), pp. 647–665. doi: [10.1016/j.physletb.2016.07.042](https://doi.org/10.1016/j.physletb.2016.07.042). arXiv: [1606.05129](https://arxiv.org/abs/1606.05129) [[hep-ex](#)].
- 1800 [57] Torbjorn Sjöstrand, Stephen Mrenna, and Peter Skands. “PYTHIA 6.4 Physics  
 1801 and Manual”. In: *JHEP* 0605 (2006), p. 026. doi: [10.1088/1126-6708/2006/05/026](https://doi.org/10.1088/1126-6708/2006/05/026). arXiv: [hep-ph/0603175](https://arxiv.org/abs/hep-ph/0603175).
- 1802 [58] *Further ATLAS tunes of PYTHIA6 and Pythia 8*. Tech. rep. ATL-PHYS-PUB-  
 1803 2011-014. Geneva: CERN, 2011. URL: <https://cds.cern.ch/record/1400677>.
- 1804 [59] Aafke Christine Kraan. “Interactions of heavy stable hadronizing parti-  
 1805 cles”. In: *Eur. Phys. J. C* 37 (2004), pp. 91–104. doi: [10.1140/epjc/s2004-01946-6](https://doi.org/10.1140/epjc/s2004-01946-6). arXiv: [hep-ex/0404001](https://arxiv.org/abs/hep-ex/0404001) [[hep-ex](#)].
- 1806 [60] M. Fairbairn et al. “Stable massive particles at colliders”. In: *Phys. Rept.* 438  
 1807 (2007), p. 1. doi: [10.1016/j.physrep.2006.10.002](https://doi.org/10.1016/j.physrep.2006.10.002). arXiv: [hep-ph/0611040](https://arxiv.org/abs/hep-ph/0611040).
- 1808 [61] W. Beenakker, R. Hopker, M. Spira, and P. M. Zerwas. “Squark and gluino  
 1809 production at hadron colliders”. In: *Nucl. Phys. B* 492 (1997), p. 51. doi:  
 1810 [10.1016/S0550-3213\(97\)00084-9](https://doi.org/10.1016/S0550-3213(97)00084-9). arXiv: [hep-ph/9610490](https://arxiv.org/abs/hep-ph/9610490).
- 1811 [62] A. Kulesza and L. Motyka. “Threshold resummation for squark-antisquark  
 1812 and gluino-pair production at the LHC”. In: *Phys. Rev. Lett.* 102 (2009),  
 1813 p. 111802. doi: [10.1103/PhysRevLett.102.111802](https://doi.org/10.1103/PhysRevLett.102.111802). arXiv: [0807.2405](https://arxiv.org/abs/0807.2405) [[hep-ph](#)].

- 1822 [63] A. Kulesza and L. Motyka. “Soft gluon resummation for the production  
 1823 of gluino-gluino and squark-antisquark pairs at the LHC”. In: *Phys. Rev.*  
 1824 *D* 80 (2009), p. 095004. doi: [10.1103/PhysRevD.80.095004](https://doi.org/10.1103/PhysRevD.80.095004). arXiv:  
 1825 [0905.4749 \[hep-ph\]](https://arxiv.org/abs/0905.4749).
- 1826 [64] Wim Beenakker, Silja Brensing, Michael Kramer, Anna Kulesza, Eric Lae-  
 1827 nen, et al. “Soft-gluon resummation for squark and gluino hadroproduc-  
 1828 tion”. In: *JHEP* 0912 (2009), p. 041. doi: [10.1088/1126-6708/2009/12/041](https://doi.org/10.1088/1126-6708/2009/12/041). arXiv: [0909.4418 \[hep-ph\]](https://arxiv.org/abs/0909.4418).
- 1830 [65] W. Beenakker, S. Brensing, M.n Kramer, A. Kulesza, E. Laenen, et al. “Squark  
 1831 and Gluino Hadroproduction”. In: *Int. J. Mod. Phys. A* 26 (2011), p. 2637.  
 1832 doi: [10.1142/S0217751X11053560](https://doi.org/10.1142/S0217751X11053560). arXiv: [1105.1110 \[hep-ph\]](https://arxiv.org/abs/1105.1110).
- 1833 [66] Michael Krämer et al. *Supersymmetry production cross sections in pp collisions*  
 1834 at  $\sqrt{s} = 7 \text{ TeV}$ . 2012. arXiv: [1206.2892 \[hep-ph\]](https://arxiv.org/abs/1206.2892).
- 1835 [67] Rasmus Mackeprang and Andrea Rizzi. “Interactions of Coloured Heavy  
 1836 Stable Particles in Matter”. In: *Eur. Phys. J. C*50 (2007), pp. 353–362. doi:  
 1837 [10.1140/epjc/s10052-007-0252-4](https://doi.org/10.1140/epjc/s10052-007-0252-4). arXiv: [hep-ph/0612161](https://arxiv.org/abs/hep-ph/0612161)  
 1838 [hep-ph].
- 1839 [68] Rasmus Mackeprang and David Milstead. “An Updated Description of  
 1840 Heavy-Hadron Interactions in GEANT-4”. In: *Eur. Phys. J. C*66 (2010), pp. 493–  
 1841 501. doi: [10.1140/epjc/s10052-010-1262-1](https://doi.org/10.1140/epjc/s10052-010-1262-1). arXiv: [0908.1868](https://arxiv.org/abs/0908.1868)  
 1842 [hep-ph].
- 1843 [69] J. Alwall, R. Frederix, S. Frixione, V. Hirschi, F. Maltoni, O. Mattelaer, H. S.  
 1844 Shao, T. Stelzer, P. Torrielli, and M. Zaro. “The automated computation of  
 1845 tree-level and next-to-leading order differential cross sections, and their  
 1846 matching to parton shower simulations”. In: *JHEP* 07 (2014), p. 079. doi:  
 1847 [10.1007/JHEP07\(2014\)079](https://doi.org/10.1007/JHEP07(2014)079). arXiv: [1405.0301 \[hep-ph\]](https://arxiv.org/abs/1405.0301).
- 1848 [70] “dE/dx measurement in the ATLAS Pixel Detector and its use for particle  
 1849 identification”. In: (2011).
- 1850 [71] ATLAS Collaboration. “The ATLAS Simulation Infrastructure”. In: *Eur.*  
 1851 *Phys. J. C*70 (2010), pp. 823–874. doi: [10.1140/epjc/s10052-010-1429-9](https://doi.org/10.1140/epjc/s10052-010-1429-9). arXiv: [1005.4568 \[physics.ins-det\]](https://arxiv.org/abs/1005.4568).

1853 DECLARATION

---

1854 Put your declaration here.

1855 *Berkeley, CA, September 2016*

---

1856

Bradley Axen



1857

1858 COLOPHON

1859

Not sure that this is necessary.